23-Apr-21

Doppler-Lidar Evaluation of HRRR-Model Skill at Simulating Summertime Wind Regimes in the Columbia River Basin during WFIP2

Robert M. Banta,[1,2] Yelena L. Pichugina[1,2], Lisa S. Darby[3], W. Alan Brewer[2], Joseph B. Olson[4], Jaymes S. Kenyon,[1,4] S. Baidar, [1,2] S.G. Benjamin[4], H.J.S. Fernando[6], K.O. Lantz[5], J.K. Lundquist[7,10], B.J. McCarty,[1,2] T. Marke,[1,2] S.P. Sandberg,[2] J. Sharp,[8] W.J. Shaw,[9] D.D. Turner,[4] J.M. Wilczak,[3] R. Worsnop,[3] M.T. Stoelinga[11,12]

[1]CIRES, University of Colorado, Boulder, CO, USA

[2]NOAA/ Chemical Sciences Laboratory, Boulder, CO, USA

[3]NOAA/ Physical Sciences Laboratory

[4]NOAA/ Global Systems Laboratory

[5]NOAA/ Global Monitoring Laboratory

[6]University of Notre Dame, Notre Dame, Indiana, USA

[7]University of Colorado, Boulder, CO, USA

[8]Sharply Focused LLC, Portland, OR, USA

[9]Pacific Northwest National Laboratory, Richland, WA, USA

[10]National Renewable Energy Laboratory, Golden, CO, USA

[11]Vaisala, Seattle WA, USA

[12]Current affiliation: ArcVera Renewables, Golden, CO, USA

Corresponding author: Robert M. Banta, NOAA/CSL, 325 Broadway, Boulder CO 80305.
robert.banta@noaa.gov

Early Online Release: This preliminary version has been accepted for publication in *Weather and Forecasting*, may be fully cited, and has been assigned DOI 10.1175/WAF-D-21-0012.1. The final typeset copyedited article will replace the EOR at the above DOI when it is published.

Abstract

Complex-terrain locations often have repeatable near-surface wind patterns, such as synoptic gap flows and local thermally forced flows. An example is the Columbia River Valley in east-central Oregon-Washington, a significant wind-energy-generation region and the site of the Second Wind-Forecast Improvement Project (WFIP2). Data from three Doppler lidars deployed during WFIP2 define and characterize summertime wind regimes and their large-scale contexts, and provide insight into NWP model errors by examining differences in the ability of a model [NOAA's High-Resolution Rapid-Refresh (HRRR-version1)] to forecast wind-speed profiles for different regimes. Seven regimes were identified based on daily time series of the lidar-measured rotor-layer winds, which then suggested two broad categories. First, in three regimes the primary dynamic forcing was the large-scale pressure gradient. Second, in two regimes the dominant forcing was the diurnal heating-cooling cycle (regional sea-breeze-type dynamics), including the *marine intrusion* previously described, which generates strong nocturnal winds over the region. The other two included a hybrid regime and a non-conforming regime. For the large-scale pressure-gradient regimes, HRRR had wind-speed biases of ~1 m s^{-1} and RMSEs of 2-3 m s^{-1}. Errors were much larger for the thermally forced regimes, owing to the premature demise of the strong nocturnal flow in HRRR. Thus, the more dominant the role of surface heating in generating the flow, the larger the errors. Major errors could result from surface heating of the atmosphere, boundary-layer responses to that heating, and associated terrain interactions. Measurement/modeling research programs should be aimed at determining which modeled processes produce the largest errors, so those processes can be improved and errors reduced.

Plain-language Summary

Evaluating the performance of NWP forecast models in complex terrain is important for many applications, but especially so for wind energy (WE), because many WE generation facilities are located in complex terrain. It is also important as part of this effort to understand wind-flow phenomena and their primary forcing mechanisms. This study used wind-profile data from three Doppler lidars deployed as part of the Second Wind Forecasting Improvement Project to investigate wind-flow phenomena in the Columbia River Basin of Oregon-Washington. By examining daily time-height cross sections and rotor-layer time series of lidar-measured winds, seven regimes are separated out based on the diurnal course of the winds. In three regimes the primary dynamic forcing was the large-scale pressure gradient across the Cascade-Mountain barrier, under upper-level troughing and with cooler afternoon temperatures in the basin. In two other regimes, the dominant dynamics were the diurnal heating-cooling cycle (regional sea-breeze-type dynamics), including the 'marine intrusion' described previously. The latter regimes occurred under upper-level ridging and hotter daytime temperatures inland. NOAA's High-Resolution Rapid-Refresh (HRRR) model was verified against the lidar profile data, and the errors were much larger for the regimes where thermal-contrast forcing dominated than for those where large-scale pressure-gradient forcing prevailed, i.e., the more dominant the role of surface heating in generating the flow, the larger the errors. The contrast in model performance between these two broad categories indicates that significant model errors are associated with mesoscale and boundary-layer dynamic processes driven by surface-heating effects. Future measurement/modeling research should be aimed at finding out which processes contribute most to these errors.

v

1. Introduction

Complex-terrain wind flow in the lowest several hundred meters of the atmosphere presents a significant forecasting challenge. The importance of this challenge has recently been elevated by needs of the wind-energy (WE) industry for accurate wind forecasts in this layer. Accurate forecasting relies on accurate NWP forecast models. Today's models have seen significant improvement over the past decades, but the ascendancy of quantitative applications such as WE have raised the required forecast accuracy beyond current capabilities.

Winds in complex terrain tend to be constrained by the topography, resulting in recurring flow patterns that are similar from case to case, which in theory should be advantageous to modeling them. On the other hand, dynamic processes in the lowest layers of the atmosphere are among the most challenging for contemporary NWP models, where interactions with the surface, sub-resolution-scale transports through the boundary layer, and representation of the earth and canopy layers—not to mention the coarse representation of the topography itself given the resolution of the model—can all be sources of significant error, all exacerbated by complex terrain. Effectively dealing with model-improvement issues requires comprehensive measurement campaigns to verify the models and diagnose significant sources of model error.

The Second Wind Forecast Improvement Project (WFIP2) was implemented to address these needs. A major WFIP2 objective was to identify and better understand the various atmospheric flow phenomena that impact the WE industry, with an ultimate goal of improving skill in

modeling and predicting wind speeds produced by each type of flow. WFIP2 had two major science components: 1) a comprehensive 18-month field-measurement campaign in the Columbia River Basin of Oregon and Washington from September 2015 to March 2017, comprising an extensive deployment of surface-based remote-sensing and tower-mounted instrumentation, and 2) verification and improvement of NOAA/NCEP's High-Resolution Rapid-Refresh (HRRR) operational numerical weather prediction (NWP) forecast model using the WFIP2 measurement dataset.

NWP models are an indispensable tool in formulating the quantitative forecasts of wind speed that the WE industry relies on. For WE operations, these forecasts are needed aloft in the layer of the atmosphere spanned by wind-turbine rotor blades, or *rotor layer*, and they need to be as accurate as possible (<0.1 m s^{-1} desirable) for forecast lead times of hours and also out to 1-2 days (Ahlstrom et al. 2013; Marquis et al. 2011; Banta et al. 2013). Wind-turbine types vary, but the rotor layer generally extends between ~40 and 150 m above ground level (AGL) for many modern land-based turbines. The HRRR model used in this study, run operationally at NCEP, is a short-term forecast model widely used by aviation, agriculture, renewable energy, severe weather, and others, because of its ability to ingest and assimilate the latest atmospheric measurement data hourly. Among the users are private-industry WE forecast providers, who use HRRR as a foundational model on which to base wind predictions, or as initial conditions for specialized, higher resolution private-industry-consultant numerical forecast models (Olson et al. 2019a,b).

Different meteorological conditions produce different diurnal patterns or regimes of wind evolution. It was anticipated that HRRR would do better at predicting some regimes than others, so an aspect of WFIP2 was to find out whether this was so, and to characterize the nature and magnitudes of the errors for each flow type. Some general wind categories have been identified in the study region. In the cold season, gap flows through the Columbia River Gorge west of The Dalles (between Troutdale and The Dalles OR; see Fig. 1) are controlled by the surface pressure difference across the Cascade Mountain barrier, as noted by Sharp and Mass (2002, 2004) and Neiman et al. (2019). Cold pools that can persist for many days in winter occur under weak winds aloft (Whiteman et al. 2001, Zhong et al. 2001, McCaffrey et al. 2019). In the present study we focus on summertime flow regimes. Gap flows forced by synoptic pressure gradients also happen in summer, but another type of gap flow often forms, due to the strong daytime horizontal temperature differences between the warm, arid interior of central Oregon-Washington and the cool Pacific Ocean waters offshore. These are thermally induced flows, which have a diurnal cycle. An example of such a recurrent flow is the *marine intrusion* described by Banta et al. (2020).

To study the marine intrusion and to evaluate HRRR's ability to model it, Banta et al. (2020) used accurate wind-profile data from three scanning Doppler lidars sited along a wind-energy corridor in the Columbia River Basin (Fig.1), taken during the summer 2016 period of WFIP2. This diurnal wind system is a result of regional sea-breeze forcing. Marine intrusions pushed through the WFIP2 study area on eight of the 92 days of June-July-August (JJA) 2016. A distinctive diurnal error signature was found in the HRRR-model simulations of marine intrusions, in which the model prematurely and routinely terminated the strong westerly intrusion

winds after local midnight (Banta et al. 2018a, 2020; Pichugina et al. 2019). These premature downramping errors also resulted in large underestimates of wind-generated power over the region (Wilczak et al. 2019). Remaining unanswered questions include: was there a typical large-scale context associated with marine intrusions, and what happened on the other days? Here we will again use wind-profile data from the three WFIP2 Doppler lidars to address these questions.

Previously, Pichugina et al. (2019) used the same three Doppler lidars to calculate annual and seasonal statistics of wind properties through the lowest 500 m of atmosphere, and annual and seasonal error statistics for the operational HRRR. The low-level winds were bidirectional: mostly westerly (250-271°), occasionally easterly (71-91°), but rarely from any other direction. Compared against the lidar measurements, HRRR annual wind speeds were biased 0.5 m s^{-1} low, largely by underestimating strong wind speeds (>12 m s^{-1}). Annual and seasonal errors in the rotor layer, further reviewed below, were not found to increase with forecast lead time. For quantities relevant to WE, Pichugina et al. (2019) showed how errors in mean annual wind speed translated to errors in annual energy production (AEP), both calculated from the wind-speed-distribution histogram. Errors in wind speed at 100 m height ranged from 5.7% to 16.5% and in AEP, from 10% to 26%.

The present study extends these analyses by breaking down the annual and seasonal statistics over all flow conditions (Pichugina et al. 2019) into several frequently occurring types of flow in summer. We provide a survey of seven flow types or regimes identified during the JJA 2016 period of WFIP2. Rotor-layer wind speeds (here a generic 50-150-m AGL mean value for the

rotor-layer average) measured at the three Doppler-lidar sites define these regimes as groupings of days having similar diurnal-evolution patterns of the winds.

2. Background, instrumentation, models

Summertime meteorology of the U.S. West-Coast states from northern California to Washington is strongly influenced by two factors, a strong persistent offshore surface-pressure ridge, and routinely hot daytime temperatures (often >30°C) over the Great Basin inland of the Cascade/Sierra-Nevada Ranges (Fig.1). Upwelling ocean waters of the north-to-south offshore current are cool (~13-14°C) and contrast with the hot daytime inland temperatures, to generate strong regional sea-breeze forcing (Staley 1959).

Banta et al. (2020) reviewed previous studies relevant to the inland penetration of marine air in this region. Fire weather was a strong motivator in many early West Coast studies, which describe the roles of the sea-breeze forcing *vs*. the cross-shore, large-scale pressure gradient in determining wildfire potential in California and Oregon to the west of the Sierra-Cascade Barrier, and air quality motivated others (Fosberg and Schroeder 1966; Schroeder et al. 1967; Olsson et al. 1973; Johnson and O'Brien 1973; Banta 1995; Zaremba and Carroll 1999; Darby et al. 2002; Wang and Ullrich 2018). Additionally, Mass et al. (1986) document surges of cool air propagating northward up the coast of Oregon-Washington, and eastward through the Washington Coastal Range and Puget Sound. These studies all describe marine air flow up to (but not over) the Cascade barrier. In studies that include wind characteristics in the arid basins *east* of the Cascades, as being investigated here, Staley (1959), Doran and Zhong (1994), and Brewer and Mass (2014) describe diurnal patterns in the surface winds, and noted bidirectional wind roses at many locations, indicating a strong control of the near-surface flow by terrain over

this region. Although semi-persistent features dominate the summertime climatology of the WFIP2 locale, it is far enough north that storm tracks carry traveling frontal and cyclonic systems through the region throughout the summer.

a. The Second Wind Forecast Improvement Project

WFIP2 took place in the Columbia River Basin, focused on an east-west corridor that contains many wind-energy-generation facilities (Fig.1b). This region is a major source of electrical energy, administered by the Bonneville Power Authority, which provides 4.6 GW of maximum-capacity power to urban centers in Oregon, Washington, and south into California (Wilczak et al. 2019). The Project—both the field-measurement deployment and the efforts to use these measurements to evaluate NWP model errors and improve models—emphasized benefits to the WE industry. The field program consisted of arrays of ground-based in-situ and remote-sensing instrumentation (eight 915-MHz wind-profiling radars, 19 Doppler sodars, five wind-profiling lidars, four scanning Doppler lidars, and four profiling microwave radiometers), along with other measurement systems. Most of these instruments were deployed for 18 months from September 2015 through March 2017, as described in the instrumentation overview by Wilczak et al. (2019). The NWP model for WFIP2 studies was the HRRR, described by Benjamin et al. (2016) and in the WFIP2 modeling overview by Olson et al. (2019a,b). Subsequent refinements in boundary-layer and other atmospheric processes in the HRRR have been developed over the last five years through HRRR version 4 (Olson et al 2019a; Bianco et al. 2019; Dowell et al. 2021).

Many wind farms are located in complex terrain to take advantage of flow accelerations and concentrations of momentum associated with terrain features, so a complex-terrain location was

chosen for WFIP2. An advantage of studying winds in complex terrain is that the low-level flow is often strongly constrained by the topography (as alluded to in the Introduction), so that some flow patterns are repeatable, such as the gap and slope flows, cold pools, and marine intrusions of the Columbia Basin. Understanding and forecasting winds consists of relating them to the dominant physical and dynamical drivers in the location of interest. A limitation of complex-terrain findings is that many results (observational and model-related) are unique to the area being studied, not transferable to other sites having different terrain. Each individual complex-terrain environment may need to have its own study to address location-specific issues and determine appropriate location-specific predictors of wind properties. Field programs such as WFIP2 are valuable because they demonstrate the benefits of conducting such comprehensive field deployments, to better understand the distinctive flow types for a specific locale and how NWP models handle them, and thereby to provide improved forecasts for that location. Such long-term, comprehensive programs help to define, demonstrate, and refine effective procedures for designing future field programs to address wind-forecasting issues for individual complex-terrain regions, especially when closely tied to careful NWP-model evaluation efforts.

To avoid starting the post-project analysis of the large volume of data with a blank slate, it was deemed important to document meteorological conditions and model performance during the experiment in near real time, while these conditions were still fresh in the researchers' minds. Project meteorologists held open, weekly, on-line briefings in which meteorological conditions, winds, and HRRR-model performance for each day were highlighted, flow types were classified, and summaries for each day were entered into an Event Log, which would serve as a reference and starting point for post-project analyses and studies (Wilczak et al. 2019). In the Event Log,

the briefer for each day checked the dominant wind-flow types, subjectively evaluated model performance and importance to WE and WFIP2 objectives for conditions on that day on a three-tiered scale (good, average, poor for model performance; high, medium, low for significance to WE), and entered a summary text of prevailing meteorological conditions. Event types defined for WFIP2 are listed in Table 1. A critical need for accomplishing in-project characterization of meteorology was near real-time access to the measurement datasets. Two web sites were available to provide this kind of timely data availability, one described by Wilczak et al. (2019), and the other described in the next section.

b. Doppler-lidar

The main instrumentation for the present study was three scanning Doppler lidars deployed to sites along the Columbia River Valley at the Wasco and Arlington, Oregon airstrips and in Boardman OR (Fig.1), as described by Pichugina et al. (2019, 2020). The lidars were deployed along a west-southwest/east-northeast line over a total distance of 71 km. We focus on Doppler lidar because of its accuracy and its ability to provide these accurate winds from a few meters above ground level (AGL) up to 2-3 km AGL or more on most occasions, and reliably to at least 800 m AGL. Evaluating difference quantities (here model errors) requires accuracy of measurement; in comparing these errors from one regime to another, we calculate differences of differences, which requires even greater measurement accuracy.

Our 15-min scanning procedure for the three lidars consisted of a repeated, simultaneous sequence of scans in azimuth and elevation for 12 min followed by 3 min of vertical staring (Table 2). All data from all conical and vertical-sector scans were combined into a velocity-

azimuth-display (VAD) analysis algorithm (Lhermitte and Atlas 1961, Browning and Wexler 1968) that produced a vertical profile of the mean horizontal winds every 15 min (Banta et al. 2002, 2015, 2018b, 2020; Pichugina et al. 2019). This profile was thus calculated from data distributed throughout what one might consider a flattened hemisphere of data points, divided into vertically stacked, horizontal disk-shaped bins, and subjected to multiple quality-assurance steps, with an accuracy of 0.1 m s^{-1} for WFIP2 as estimated by Pichugina et al. (2019); see also Klaas et al. (2015). This procedure provides a profile averaged over space and time in a manner similar in many respects to that generated by an NWP model (Skamarock 2004). Interested readers are referred to Pichugina et al. (2019) or Banta et al. (2020) for more in-depth details about the Doppler-lidar scanning and processing procedures.

In order to use the quantitative lidar wind-profile data to maximum advantage in real time during WFIP2, especially with respect to the event-logging activities, an innovative web page provided time-height cross sections of wind speed and other related quantities every 15 min, updated within 2 min of the end of each 15-min averaging period, plotted for the previous 12 h. Examples of several kinds of display available on this web site are shown in Fig.2. To facilitate the association of model errors with meteorological conditions as they were happening in real time, time-height HRRR-output wind values (saved hourly) were plotted next to lidar wind speeds (re-averaged to hourly for comparison with the model). Model-minus-lidar differences (errors) were calculated and also presented as color-coded time-height cross sections for the previous 12 h (Fig.2e). Quantitative differences can sometimes be smeared, obscured, or amplified by color scales, so time-series and vertical-profile curves of the variables of most interest—rotor-layer wind speed and model error—were also provided on the web site to allow a quantitative

assessment of flow conditions and HRRR errors (Fig.2c,d,f). Model-related wind and error quantities (Fig.2e,f), available every hour, were posted within minutes of the top of the hour. Event loggers found this site to be valuable in providing quantitative information on details of flow structure in the lowest several hundred meters AGL, such as layer depths, shear zones, and LLJ properties, as well as circumstances and magnitudes of significant model errors.

c. HRRR model

We use forecast output from the operational HRRR, produced by NCEP during WFIP2, to maximize the sample size of each regime studied. Nested within the Rapid-Refresh (RAP) model (13-km grid), HRRR-NCEP is an hourly updated NWP model that runs 24/7 on a 3-km horizontal grid over a domain that encompasses the continental U.S. (see maps in Olson et al. 2019b; Pichugina et al. 2020). This was HRRRv1 as described in greater detail by Benjamin et al. (2016) and Pichugina et al. (2019), and interested readers are referred to those sources for more detailed information.

Sea-surface temperature (SST) is an important quantity for sea-breeze dynamics. HRRR's SST is initialized from Global Forecast System (GFS) model values, and held fixed for the duration of the run. In 2016 GFS values were assimilated from NCEP's daily high-resolution, real-time, global, sea-surface-temperature (RTG_SST_RT) analysis (Thiebaux et al. 2003), which was based on AVHRR satellite data supplemented by ship and buoy information. These HRRR SSTs have not been systematically verified against data.

A few studies have verified HRRR wind-speed profiles, including the rotor layer, against measurements. Pichugina et al. (2019) used WFIP2 wind data from the three lidars, finding root-mean-square errors (RMSE) of 3 m s^{-1}, mean absolute errors (MAE) of 2.2 m s^{-1}, and low biases

of ~0.4 m s^{-1} for rotor-layer, annually averaged, 3-h-forecast values, which increased with height through the rotor layer from smaller values near the surface. Results of similar magnitude were reported by Olson et al (2019), Bianco et al. (2019), and Pichugina et al. (2020), who used WFIP2 test runs including HRRRv1 ('HRRR-control') for four 6-week periods (one for each season) during 2016. The first two of these studies calculated MAE and bias for the 80-m height AGL and verified against a different mix of measurements from the Pichugina et al studies, including sodar and wind-profiling radars. Consistent with Pichugina et al. (2019), these studies found larger-magnitude errors at night and in summer. Earlier, Benjamin et al (2016) verified RAP against rawinsonde, finding a 2.5 m s^{-1} difference in (the scalar) wind speed. Djalalova et al. (2016), Pichugina et al. (2017), and Banta et al. (2018) performed a series of HRRR-evaluation studies for data taken during a July-August 2004 field program in coastal New England, which included shipborne, offshore wind-profile measurements over the Gulf of Maine. RMSEs were 2.0-2.5 m s^{-1}, varying by time of day and height, increasing with lead time to >3 m s^{-1} for forecasts out to 8-h or longer.

Olson et al. (2019) also compared HRRR output with METAR (surface) measurements over a 4-yr period August 2014—August 2018. For the western U.S. stations, RMSEs ranged between 3.0 and 3.5 m s^{-1}, the largest values in summer, and biases were less than +0.3 m s^{-1}, largest also in summer. Using HRRRv2, Lee et al. (2019) showed wind-speed errors ranging from 1 to 2 m s^{-1} at 10 m height for three selected months of data between September 2016 and April 2017 in Alabama. Fovell and Gallagher (2020) performed goodness-of-fit regression analyses of HRRRv3 initial and 24-h forecasts against standard surface measurements over the U.S. and against rawinsonde winds above 250 m AGL from December 2018 through July 2019, finding good agreement. Comparison with surface measurements showed low biases mostly less

than 1 m s^{-1} in magnitude that became more negative with wind speed, i.e., HRRR "underestimated the wind speeds at windier locations." In contrast, comparisons with rawinsonde data showed overestimates of wind speed in the 280-440-m layer by 1 m s^{-1}, increasing with wind speed.

These studies taken together indicate representative HRRR RMSE values of approximately 3 m s^{-1} and biases of generally 0.5-1.0 m s^{-1} in magnitude overall.

d. Preliminary pressure-difference analyses

The most intuitive control on wind speeds through the Columbia Valley is the east-west component of the near-surface pressure difference across the Cascade barrier. Banta et al. (2020) composited this pressure difference for several NWS station pairs for the eight marine-intrusion days, focusing on the pressure (altimeter-setting) difference between a coastal site, Astoria OR (AST in Fig.1) and a site in the Columbia Basin, Hermiston OR (HRI). The diurnal variation of this Astoria-Hermiston pressure difference Δp_{AH} follows a curve that appears nearly sinusoidal, displaced upward due to the larger-scale pressure gradient imposed by the offshore ridge. As a first step in looking at all summer days, Fig.4a shows this difference for all JJA days of 2016. It is clear that the envelope bracketing most of the days, as well as the composite mean, exhibits the typical near-sinusoidal behavior, and most individual days also show this behavior. Fig.4b shows the next logical analysis step: plotting the maximum daily rotor-layer wind speed against the daily mean of this pressure difference.[1] The large scatter shows that the relationship is not

- - - - - - - -

1–Daily maximum pressure differences were also plotted with the same inconclusive result.

simple. Broadly, in the real atmosphere at any given location, conditions are controlled by processes acting at multiple time and distance scales: real-world, every-day meteorology is "messy." The challenge is to use measurements to adequately characterize the atmosphere in a region of interest and to define conditions in which useful generalizations can be made, and quantitative physical and dynamic relationships defined.

3. Results: Data analysis

To refine the analysis, we used the daily wind patterns at the three lidar sites to group the days. We then considered other data and analyses to clarify the larger-scale context, as we will describe in subsection b.

a. Defining the regimes using Doppler-lidar wind analyses

Daily Doppler-lidar time series and time-height cross sections of rotor-layer wind speed were used to group days according to similar patterns of wind behavior, initially subjectively. The first group, the marine intrusion, was defined previously by Banta et al. (2020), based on three consecutive days in June 2016 and four days in a row in August, which exhibited nearly identical diurnal periodicity. Including this one, we found seven groupings or regimes as shown in Table 3, which also itemizes quantitative criteria, applied to discriminate among the groups. Appendix Table A1 lists the days included in each regime along with the Event Type given in the Event Log. Some days are uncategorized, because of significant disruptions of the daily wind pattern,

Accepted for publication in *Weather and Forecasting*. DOI 10.1175/WAF-D-21-0012.1.

for example by precipitation systems. Inclusion or exclusion of marginal days in any of these regimes would not affect the overall findings of this study.

The regimes. Figure 4 shows examples of time-height cross sections, and Fig.5, time series, for two of the regimes, the marine intrusion, and a weaker-wind regime that also shows a diurnal increase of westerly momentum at night. As defined by Banta et al. (2020), the MARINE INTRUSION has a burst of westerly flow in late afternoon to >10 m s^{-1} in the rotor layer,[2] and minimum wind speeds (specified as <3 m s^{-1} at Arlington) during the local previous-afternoon hours (Figs.4a,5a). The second regime began with easterly winds in the afternoon and early evening local time, then shifted to westerly in the middle of the night, and back to easterly midmorning (Figs.4b,5b); we refer to this as the East-West-East (EWE) regime. As the winds in this locale are only from one of two directions, west or east, we defined easterly speeds as negative, as in Fig.5b, for purposes of regime characterization. For this regime the impressed larger-scale, east-west pressure gradients (shown later) were small, but the cross-barrier Δp_{AH} seldom actually went negative. So it is likely that the easterly daytime winds were generated by easterly mountain-plains-circulation forcing between the Cascade Range and the Columbia Basin; these circulations were able to develop because of the weaker large-scale pressure gradients across the region. A small group of three EWE days had larger values of Δp_{AH}, westerly windspeeds stronger and of longer duration, and briefer periods of easterly flow, than

- - - - -

2–Specifically, the criteria were: wind speeds >10 m s^{-1} for at least 6 h at Wasco, 3 h at Arlington, and 1 h at Boardman.

316 the other EWE days. These days of intermediate properties have been separated out as a
317 subgroup for some parts of this analysis, where they are referred to as EWE-plus (EWE+) days.

318

319 Figure 6 shows rotor-layer windspeed time series for three regimes generally associated with
320 synoptic or other larger-scale forcing. On some days the winds would begin at low speeds and
321 increase through the day, ending at >10 m s^{-1}. This UP-trending of wind speeds often occurred
322 with cold-frontal passages, but they could also be associated with smaller-scale features such as
323 the "surge" of Mass et al. (1986). UP days were often followed by one or more days when the
324 wind speeds were strong and westerly all day. Defined as days when the minimum daily rotor-
325 layer wind speeds at Arlington or Boardman (or both) did not drop below 5 m s^{-1} for periods of
326 more than 15 min,[3] we refer to these days as Strong Westerly (STRONG-W or "W!") days. As the
327 postfrontal synoptic trough pattern shifted eastward out of the region, the UP and W! days would
328 yield to DOWN-trending days. A curious feature of the DOWN days was their similarity to the
329 INTRUSION-regime pattern: they began with strong winds between 00 and 03 UTC, greater than
330 10 m s^{-1}, and often greater than 15 m s^{-1}, then declined steadily to small values during afternoon
331 hours. What distinguished the wind pattern of the DOWN days from the INTRUSION days was the
332 absence of minimum wind speeds <5 m s^{-1} at any site on the afternoon prior to the DOWN day,
333 i.e., the minimum wind speeds stayed greater than 5 m s^{-1}at all three sites after 12 UTC on the
334 previous day.

335 - - - - -

3–Winds at Boardman were lighter and more variable than other sites, so even on strong-wind days, occasional brief lulls occurred.

A sixth type (Fig.7a,b) also exhibited a diurnal pattern having timing similar to the INTRUSION pattern, but one where either the wind speeds did not meet the >10 m s^{-1} maximum criterion, or, more often, did not meet the <3 m s^{-1} minimum at Arlington. We call this grouping the COOL-DIEL regime, as described later in subsection b. The seventh regime is the NO-DIEL regime, where the diurnal pattern of strong winds at night and weaker winds during the day was not evident (Fig.7c). Many different types of flow are in this group, for example two of the days had easterly winds all day (or nearly so: Fig.7d).

Regime time-series composites. Figure 8 shows composite-mean diurnal time series of windspeed for each of the regimes using 15-min lidar data, along with the composite standard deviation σ_v for each 15-min period. On the UP-trending days, the flow accelerations could occur at any hour, so the hourly σ_v's were sometimes large, approaching 5 m s^{-1} for some time periods. The W! days indicate a tendency toward stronger winds in late afternoon and at night than earlier in the daytime (Wasco and Arlington), similar to the normal diurnal pattern. In spite of a range of westerly wind speeds for W!, the σ_v's were relatively modest, generally ~2-3 m s^{-1}, significantly smaller than the composite mean winds of >10 m s^{-1}. The DOWN days showed a surprisingly uniform daily pattern, where composite mean winds declined from 15 to 5 m s^{-1}, at similar timing over the course of the day from case-to-case, resembling that of the INTRUSION days as mentioned. The regular pattern of each realization and the small 1½ -2 m s^{-1} σ_v's of the DOWN days, suggest that diurnal-cycle forcing had a role in the eastward ejections of the cool air masses near the surface. The NO-DIEL days represented a mixture of flow types, as reflected in the large values of σ_v relative to the mean.

- - - - -

4–*Diel* means having a 24-h period, synonymous with the way meteorologists use the term "diurnal."

Accepted for publication in *Weather and Forecasting*. DOI 10.1175/WAF-D-21-0012.1.

On each of the eight marine-intrusion days (Fig.8e) the flow evolved in a similar way, so that the standard deviations were small, mostly 2 m s^{-1} or less, and often less than 1 m s^{-1}. The largest σ_v values here were due to differences in time of onset (Banta et al. 2020). The EWE regime also had small σ_v, of generally 2 m s^{-1} or less, largely because the winds themselves were weak. The COOL-DIEL regime days had modest σ_v values of 3 m s^{-1} through the day. The mean winds followed the normal diurnal pattern, varying from 10-12 m s^{-1} at night to 5-7 m s^{-1} during the afternoon, and individual days followed this pattern and timing.

b. Extended analysis: Characterizing the regimes

Knowledge of the larger-scale meteorological conditions accompanying a regime is useful for forecasting and important for a complete characterization of the atmosphere when each regime occurs. The near-surface horizontal pressure difference across the Cascade barrier and the positioning of long-wave ridge-trough patterns are important controls on the low-level winds in the Columbia Basin.

Diurnal behavior of pressure difference for each regime. The thick black line in each panel of Fig.9 shows the nearly-sinusoidal mean pressure-difference Δp_{AH} curve, composited for the 92-day JJA period, from Fig.3a, and the black dotted line shows the composited hourly standard deviations σ_p. The curves for each regime are color coded, with solid for the mean Δp_{AH} and dotted for the regime-composite σ_p. As a result of the inland daytime heating, and in spite of different degrees of synoptic forcing, the composites of Δp_{AH} in Fig.9 show a diurnal curve similar to JJA's for most of the regimes—including the W! and DOWN groupings where synoptic

forcing was the strongest influence (but not the only one). Δp_{AH} maximized in late afternoon (generally 00-02 UTC) for all regimes, although the EWE, UP, and the diverse NO-DIEL regimes had a flatter trend from 00-15 UTC than the other regimes. Except for these last three regimes, the peak-to-peak amplitudes of each regime were similar at ~4 hPa. Differences appeared in the timing of the maximum value and in the upward displacement along the vertical axis due to the imposed large-scale pressure gradient.

The day-to-day variability (σ_p: dotted lines) was 3 hPa for the 3-mo JJA sample, and within-regime σ_p's were 2-3 hPa for most regimes, except for the INTRUSION and EWE+ regimes (Fig.9b), where the variability was quite small: $\sigma_p \leq 1$ hPa for much of the day. The latter regimes were dominated by thermal forcing and were noticeably more consistent from case to case than the others that were more synoptically influenced. The INTRUSION and EWE+ days had also exhibited the smallest hourly variability in wind speed σ_v (Fig.8), showing that the diurnal evolution of the winds and pressure gradients was remarkably similar case-to-case within these regimes. Each day strongly resembled the others in its regime. The σ_p for the weak-wind, purely EWE days exceeded the mean values, which were small for most hours, similarly to the winds for this regime (*cf*. Fig.8).

Regime wind speed vs. Δp_{AH}. Figure 10 shows a revised version of the pressure difference Δp_{AH} *vs.* wind-speed scatter plot shown above in Fig.3b, where each datum is now color coded according to its regime. Daily maximum westerly-component speeds are indicated by circles. For those days that have periods of easterly flow, such as the EWE days, we have also plotted the minimum westerly-wind speed values (such as shown by the red dots on Fig. 5b and 7) as corresponding squares, representing the peak easterly gap flow on those days. The plot shows wind data for the three sites averaged together, but those for the individual sites (not shown) are

similar. The thermally dominated INTRUSION and EWE data points (red and orange circles) seem to fall along one line, and the three attributed to synoptic forcing (UP, STRONG-W, DOWN: blues and purple dots) cluster along another line where the winds were stronger for a given value of Δp_{AH}. The COOL-DIEL days, representing hybrid conditions, generally fall between them. For the EWE data plotted, the minimum (maximum-easterly) speeds show a weaker sensitivity to Δp_{AH}. Unsurprisingly, the diverse NO-DIEL sample data are scattered about. Days when precipitation occurred, overplotted by triads, show no systematic influence on these relationships. The most significant aspect of this analysis, however, is the clustering of thermally forced regime days and synoptically forced days along separate lines, which transforms the diffuse relationship between pressure difference and low-level wind speed in Fig. 3b into two potentially useful relationships depending on which forcing mechanism is dominant.

Figure 11a shows the same plotting of points, except color coded by the height of the 500-hPa surface h_{500} (averaged for SLE, UIL, and OTX). It is apparent that the INTRUSION and EWE groupings are associated with ridging (larger values of h_{500}), and the UP, W!, and DOWN groups were generally associated with troughing (smaller h_{500}), although some instances of higher h_{500} are seen in these synoptic groups at larger Δp_{AH} and wind speeds. A clearer distinction between the two groups can be seen when the data are color coded by maximum afternoon temperature T_{max} in the Basin at HRI (Fig.11b). INTRUSION and EWE days were characterized by afternoon temperatures that exceeded 92°F (33.3°C), whereas for UP, STRONG-W, and DOWN days, T_{max} generally did not reach 90°F (32.2°C). INTRUSION days had been defined based on their daily rotor-layer-wind behavior (Banta et al. 2020), and in undertaking the broader JJA analysis, we expected to find other days that would qualify. Only one other day (June 7) came close, but it is excluded because of a cold-frontal passage late in the day. Figures 8-11 show that the Marine

Intrusion is a well-defined phenomenon, not only because of similarities in diurnal wind behavior, but also because of the compact clustering of its days on the wind-speed/pressure-difference plot and its association with ridging and hot temperatures. Each individual MARINE-INTRUSION occurrence exhibited similar characteristics and mostly small deviations from the 8-day composite.

The other days that exhibited a distinct diurnal wind cycle, but did not qualify as an INTRUSION, also had cooler T_{max} values that did not reach 90°F—the reason for naming this regime "COOL DIEL."

Figure 12 shows the 3-month time series of h_{500} and T_{max} for JJA, where dots are plotted to show 1 July and 1 August. Major periods of troughing and cool temperatures are seen in June and July, and briefly in early August. Ridging in late June and late July led to occurrences of marine-INTRUSION (28-30 June and 26 July) and EWE days, and the four-day 14-17 August INTRUSION episode occurred during the longest ridging period of the summer, with accompanying hot inland temperatures.

Reanalysis composites. Fig.13 shows composite reanalysis charts for the sea-level pressure (SLP), 925-hPa temperature, and 500-hPa height for each regime, and for the 92-day JJA composite, to illustrate the connections between the regimes and their larger-scale context. The reanalysis images are derived from the Kalnay et al. (1996) dataset. Color-scale values, shown for the JJA charts, are the same for each regime. The JJA SLP composite shows the summertime offshore high-pressure center and inland thermal troughing extending northward through Nevada. The composites at 500-hPa show a somewhat zonal pattern with a tendency for

troughing at the Coast and ridging over the Rocky Mountains, and at 925 hPa, warm temperatures inland over the Great Basin and cool temperatures offshore.

Associated with the thermally induced INTRUSION and EWE regimes was the 500-hPa ridging pattern situated over the West and the Pacific Northwest. The offshore surface ridge over the Pacific Ocean extended well north into British Columbia (BC). Warm temperatures at 925 hPa for the INTRUSION group extended the farthest north of any regime. For the EWE regime, a lobe of high surface pressure extending eastward from BC through Montana and Wyoming was accompanied by cool temperatures at 925 hPa (indicative of a cool air mass) over and to the east of Alberta, Montana, and Wyoming. The high-pressure lobe neutralized or even reversed the normal east-west pressure gradient along the Oregon-Washington border, which includes the WFIP2 study area, allowing the easterly flow to develop over the Columbia Basin.

From the synoptically dominated UP to the W! regimes, the 500-hPa patterns show the characteristic trough for these categories pushing southward along the coast of BC, then passing east of the Canadian Rockies for the DOWN regime. This succession is consistent with the notion that the UP regime was often associated with a cold frontal passage, the STRONG W, with postfrontal winds beneath the trough, and the DOWN, with the eastward departure of the cold air. Cool 925-hPa temperatures offshore extended well south to Vancouver Island, and temperatures inland over Montana and Wyoming were cooler than for the INTRUSION regime. For the W! cases, the synoptic westerly-wind forcing at the surface was due to strengthened low pressure inland, most intense to the lee of the Rocky Mountains, and all three synoptic regimes show a strong east-west SLP gradient along the Oregon-Washington border. The COOL-DIEL regime was similar to the three synoptic regimes in having a trough at 500 hPa and considerably cooler temperatures at 925 hPa over Washington and Oregon than was the case for INTRUSION and

EWE. The east-west SLP gradient along the Oregon-Washington border, however, was much weaker than for those other three synoptic regimes, which is most likely why the winds were able to develop a stronger diurnal signal. The NO-DIEL regime is shown for completeness.

4. Results: HRRR error evaluation

Time-height cross sections of hourly-averaged lidar wind speeds and HRRR-modeled wind speeds for the 3-h lead-time forecast are composited for the INTRUSION and STRONG-W regimes in Fig. 14, which also shows the model bias, unbiased RMSE, and total RMSE. Time-height error composites for all regimes are given in the online supplemental material. Figure 14a shows the diurnal error pattern for the INTRUSION regime. The strong INTRUSION winds at Arlington and Boardman were ended prematurely by the model in the lowest 500 m AGL, and at Wasco above 150 m, producing large low (negative) biases of more than 4 m s^{-1} and RMSE of similar magnitude. This same pattern can be seen in the EWE+ and COOL-DIEL error composites (see online supplemental Figures), but at smaller magnitudes because of the weaker winds involved. The fact that these regimes all show similar timing in their diurnal error patterns is a reason why the summertime seasonal (and the annual) error pattern qualitatively resembles the INTRUSION pattern (Pichugina et al. 2019, Banta et al. 2020).

Errors for the synoptic-dominated STRONG-W regime in Fig. 14b showed better skill but less consistency, especially site to site, than the more diurnally forced regimes. For example, strong winds lasted through the morning transition (08-18 UTC) in the lidar data and in the model at Wasco and Arlington but not in the model at Boardman, where the stronger winds in HRRR disappeared after 08 UTC, leading to large bias and RMS errors of > 4 m s^{-1}. [Large errors above 600 m at Boardman were due to weak lidar signal and spurious wind values, and have been

ignored in subsequent analyses (see discussion in Pichugina et al. 2020)]. Errors for the UP and DOWN regimes were of similar magnitude and similarly site dependent (see Supplementary Figures).

A more quantitative view of the model errors in the rotor layer is seen in the wind-speed time series in Fig. 15. Considering the synoptic regimes first (Fig.15-top), biases for the W! and DOWN regimes were relatively small (less than 1 m s^{-1}) for most hours, and the RMSE were 2-3 m s^{-1}. Because the wind-speed accelerations for the members of the UP regime occurred at different hours, it was timing errors that mostly accounted for high biases > 2 m s^{-1} at Wasco, and low biases of 4-5 m s^{-1} along with RMS errors >4 m s^{-1} at Boardman during nighttime and morning hours (07-16 UTC), which were found through a deep layer (Supplementary). The NO-DIEL regime had small biases similar to the W!, and similar RMSE of 2-3 m s^{-1} at all sites.

The regimes more influenced by diurnal forcing (Fig.15b), exhibited larger errors. Early arrival of the strong intrusion flow at Boardman overpredicted the wind speeds and generated large RMSE at 03 UTC due to timing errors, as also noted in Banta et al. (2020). Negative (low) biases exceeding 3 m s^{-1} in magnitude at Arlington and Boardman were a result of HRRR's premature termination of the intrusion flow (occurring above the rotor layer at Wasco). These biases were the primary reason for large RMSE (and MAE), as the unbiased-RMSE's (RMSEu's) were less than 2 m s^{-1}. Large errors of like behavior are also evident for EWE+. Errors for EWE showed similar timing but smaller-magnitude: RMSE mostly less than 2 m s^{-1}. However, these EWE errors were of about the same magnitude as the wind speeds, indicating the relative errors were significant. For WE purposes, accurate forecasting of weak-wind days can be important in scheduling wind-turbine down times, such as hardware maintenance, and HRRR did predict

weak winds for these days. The COOL-DIEL regime, a blend of synoptic and diurnal forcing, showed errors of similar sign and timing, but smaller than the INTRUSION and EWE+ errors.

Vertical error profiles in Fig. 16 show that the errors noted in the time series were mostly independent of height up to at least 600 m. The major exception was the INTRUSION regime, where the largest errors were at Arlington and Boardman below 400 m AGL and at night (not shown), and above 150 m at Wasco, due to the premature demise of the intrusion flow. The hour-by-hour behavior of the HRRR profiles *vs*. those measured by the three lidars for this regime is given in Banta et al. (2020: see Fig.12 of that paper). Errors were also somewhat larger aloft at 300 m for the UP and DOWN regimes and for the W! regime at Boardman.

Measured and modeled Astoria-Hermiston pressure differences are shown in the upper panels of Fig.17, and the lower panels show the HRRR errors in predicting these differences. For the synoptically dominated regimes (left), the magnitude of the HRRR errors in Δp_{AH} was less than 0.5 hPa. These gradients were overpredicted during the nighttime hours and underpredicted or small during daytime. The NO-DIEL composites showed a similar error trend but reaching twice the magnitude. For the thermally dominated regimes (right panels) HRRR also overestimated the pressure difference during late afternoon and evening, and underestimated this difference for most of the daytime. The late-afternoon overestimates of Δp_{AH} reached 1 hPa or more, which may contribute to the early-arrival mistiming of the intrusion front by HRRR.

For some regimes, such as the thermally dominated groups, the errors in wind speed were larger than desired for WE forecasting. However, the errors were repeatable within regime. Fig. 11b suggests that T_{max} is one indicator of which regime will prevail. If T_{max} could be accurately predicted (along with Δp_{AH}), one could forecast the regime, and adjust the wind-speed forecast to

Accepted for publication in *Weather and Forecasting*. DOI 10.1175/WAF-D-21-0012.1.

account for the error pattern for that regime. Figure 18 shows a scatter diagram of measured *vs*. HRRR-predicted T_{max} for HRI, color coded for each regime. The scatter is large. This version of HRRR does not seem to have sufficient skill in predicting T_{max} to be useful in forecasting regime occurrence.

5. Conclusions

For the many wind plants located in complex terrain, understanding local effects on the wind flow, both dynamic and thermodynamic, is essential. Flows through the complex terrain of the Columbia River wind-energy corridor are strongly controlled by topography, as evidenced by the bidirectional wind distributions in the lowest few hundred meters. Winds in the corridor were also controlled by the west-east, cross-barrier pressure difference across the Cascade Range. This pressure difference has two components, one imposed by the larger scale and the other diurnal due to regional thermal, sea-breeze-type forcing. The relationship between this pressure difference and the wind speed was not simple or straightforward, but taking into account the balance between these two mechanisms provided insight as to how to view this seemingly diffuse relationship.

Under the influence of upper-level troughing, related to the movement of cold fronts and cold air masses, large-scale pressure gradients dominated the forcing. The large-scale gradients and associated winds aloft varied from day to day. As a consequence of the connection between the larger-scale conditions aloft and the low-level flow, the rotor-layer wind speeds also varied from day to day (composite σ_v ~ 2-3 m s^{-1} for W!) , indicating they were sensitive to the larger-scale forcing. The large-scale context for pressure-gradient dominated flow thus consisted of troughing at 500 hPa and cooler inland temperatures of ≤90°F.

Under upper-level ridging, regional thermal-diurnal forcing dominated. Anticyclonic conditions in summer were associated with hot daytime near-surface temperatures east of the Cascades, subsidence aloft, and cloud-free skies. The large-scale gradients and associated winds aloft again varied from day to day, but the traits of the regional sea-breezes that developed were largely insensitive to differences in winds aloft (Banta et al. 2020), indicating weak connection between rotor-layer winds and the larger scale. Dominated by local forcing, individual marine intrusion events were very similar to each other. Interestingly, their associated HRRR errors were also similar.

Even under such ridging conditions, larger-scale pressure gradients in the lowest few hundred meters were imposed across the Cascade barrier, due to the seasonally persistent offshore surface ridge. When the imposed pressure gradient was strong enough, this combination of local plus large-scale forcing produced a regional sea-breeze pulse energetic enough to push through the Cascades and into the Oregon-Washington interior, resulting in the 10-15+ m s^{-1} maximum winds of the marine intrusion. The large-scale context for a marine INTRUSION thus consisted of ridging at 500 hPa that produced inland temperatures of >90°F plus an Astoria-Hermiston pressure difference Δp_{AH} > 6 hPa (Fig.9-13). Weaker cross-barrier pressure differences produced weaker EWE-type responses.

Did HRRR do a better job predicting rotor-layer wind speeds for some wind regimes than others? Yes. The synoptically dominated regimes overall showed smaller errors than those generated primarily by thermal-contrast forcing. The STRONG-W and DOWN regimes had biases of <1 m s^{-1} for much of the diurnal cycle, RMSE of ~2 m s^{-1}, and relative errors of 20%. The thermally forced regimes showed larger errors (absolute errors of >4 m s^{-1} for the INTRUSION cases and relative errors of 50% for EWE). Thus, HRRR errors were larger when diurnal thermal

forcing was involved—the more dominant the role of thermal forcing in generating the winds, the larger the errors.

From the strong role of thermal forcing in generating errors we can deduce that significant model errors are associated with surface heating and the complex-terrain boundary-layer's response to that heating—primary drivers of sea-breeze dynamics. HRRR's difficulty in predicting T_{max} in the Columbia Basin supports this inference. Specific links in the chain of processes that need to be properly modeled include, for example, components of the surface energy balance (including radiation, soil, and canopy effects, etc.), processes that heat the CBL and generate horizontal pressure gradients, processes that abet or inhibit interaction with larger scale, and others. For model improvement, therefore, a recommendation would be that future joint measurement/modeling research projects should be aimed at sorting out which of these processes contribute most to model errors, and how these processes should be represented in models.

Acknowledgments. The authors thank the WFIP2-experiment participants who aided in the deployment and the collection of lidar data. Special thanks go to our colleagues Clark King (PSL), Ann Weickmann (CSL), and Aditya Choukulkar for their preparation and deployment of lidars to the research sites. From NOAA/ESRL we thank: Roy Miller (CSL), Melinda Marquis (GSL), and Chris Clack. Thanks also to Dr. Caroline Draxl for providing the base map for Fig. 1a. This work was sponsored by the NOAA/CSL Air Quality Program, the Atmospheric Science for Renewable Energy (ASRE) Program, in part by the NOAA Cooperative Agreement with CIRES, NA17OAR4320101, and NOAA was funded in part by the U.S. Department of Energy, Wind Energy Technologies Office, via DOE grant number DE-EE0007605. Notre Dame Lidar

603 deployment was funded by the grant DOE-WFIFP2-SUB-001. Vaisala, Inc. (M.T. Stoelinga), by
604 DOE Contract No.: DE-EE0006898.

605

606

607

608 **APPENDIX**

609 Table A1: Days Included in Each Wind Regime

610

References

Ahlstrom, M., D. Bartlett, C. Collier, J. Duschesne, D. Edelson, A. Gesino, M. Keyser, D. Maggio, M. Milligan, C. Moehrlen, J. O'Sullivan, J. Sharp, P. Storck, and M. Rodriguez, 2013: Knowledge is power. *IEEE Power & Energy Magazine*, **11**, 45-52, doi: 10.1109/MPE.2013.2277999.

Banta, R.M., 1995: Sea breezes shallow and deep on the California coast. *Mon. Wea. Rev.*, **123**, 3614-3622, doi.org/10.1175/1520-0493(1995)123<3614:SBSADO>2.0.CO;2

_____, R.K. Newsom, J.K. Lundquist, Y.L. Pichugina, R.L. Coulter, and L. Mahrt, 2002: Nocturnal low-level jet characteristics over Kansas during CASES-99. *Boundary-Layer Meteor*., **105**, 221-252; https://doi.org/10.1023/A:1019992330866

_____, _____, N.D. Kelley, W.A. Brewer, and R.M. Hardesty, 2013: Wind-energy meteorology: Insight into wind properties in the turbine rotor layer of the atmosphere from high-resolution Doppler lidar. *Bull. Amer. Meteor. Soc.*, **94**, 883-902. doi.org/10.1175/BAMS-D-11-00057.1

_____, _____, W.A. Brewer, J.K. Lundquist, N.D. Kelley, S.P. Sandberg, R.J. Alvarez, R.M. Hardesty, A.M. Weickmann, 2015: 3-D volumetric analysis of wind-turbine wake properties in the atmosphere using high-resolution Doppler lidar. *J. Atmos. Oceanic Technol.*, **32**, 904-914, doi:10.1175/JTECH-D-00078.1.

_____, _____, _____, et al., 2018a: Evaluating Model Skill at Predicting Recurrent Diurnal Summertime Wind Patterns in the Columbia River Basin during WFIP-2 . *Ninth Conference on Weather, Climate, and the New Energy Economy*, Austin TX, 8 January 2018; https://ams.confex.com/ams/98Annual/videogateway.cgi/id/44388?recordingid=44388&uniqueid=Paper331274&entry_password=345478

_____, _____, _____, E.P. James, J.B. Olson, S.G. Benjamin, J.R. Carley, L. Bianco, I.V. Djalalova, J.M. Wilczak, M.C. Marquis, J. Cline, and R.M. Hardesty, 2018b: Evaluating and improving NWP forecasts

for the future: How the needs of offshore wind energy can point the way. *Bull. Amer. Meteor. Soc.*, **99**, 1155-1176, doi: 10.1175/BAMS-D-16-0310.1

_____, _____, _____, A. Choukulkar, K.O. Lantz, J.B. Olson, J. Kenyon, H.J.S. Fernando, R. Krishnamurthy, M.T. Stoelinga, J. Sharp, L.S. Darby, D.D. Turner, S. Baidar, and S.P. Sandberg, 2020: Characterizing NWP model errors using Doppler-lidar measurements of recurrent regional diurnal flows: Marine-air intrusions into the Columbia-River Basin. Mon. Wea. Rev., 148, 929-953; doi.org/10.1175/MWR-D-19-0188.1

Benjamin, S. G., S.S. Weygandt, J.M. Brown, M. Hu, C. Alexander, T.G. Smirnova, J.B. Olson, E. James, D.C. Dowell, G.A. Grell, et al., 2016: A North American hourly assimilation and model forecast cycle: The Rapid Refresh. *Mon. Wea. Rev.*, **144**, 1669-1694, doi: http://dx.doi.org/10.1175/MWR-D-15-0242.1.

Bianco, L., I.V. Djalalova, J.M. Wilczak, J.B. Olson, et al., 2019: Impact of model improvements on 80 m wind speeds during the second Wind Forecast Improvement Project (WFIP2). *Geosci. Model. Dev.*, **12**, 4803-4821; doi.org: 10.5194/gmd-12-4803-2019

Brewer, M.C. and C.F. Mass, 2014: Simulation of summer diurnal circulations over the northwest United States. *Wea. Forecasting*, **29**, 1208-1228. doi.org/10.1175/WAF-D-14-00018.1

Browning, K.A. and Wexler, R., 1968: The determination of kinematic properties of a wind field using Doppler radar. *J. Appl. Meteor*., **7**, 105-113. doi.org/10.1175/1520-0450(1968)007<0105:TDOKPO>2.0.CO;2

Darby, L.S., R. M. Banta, and R.A. Pielke, 2002: Comparisons between mesoscale model terrain sensitivity studies and Doppler lidar measurements of the sea breeze at Monterey Bay. *Mon. Wea. Rev*., **130**, 2813-2838, doi:10.1175/2002MWR2275.1

Dowell, D.C., C.R. Alexander, E.P. James, S.S. Weygandt, S.G. Benjamin, G.S. Manikin, B.T. Blake, J.M. Brown, J.B. Olson, M. Hu, T.G. Smirnova, T. Ladwig, J. Kenyon, and R. Ahmadov, 2021: The High-Resolution Rapid Refresh (HRRR): An hourly updating convection-permitting forecast model. Part I: Motivation and system description. *Mon. Wea. Rev*., manuscript in preparation.

Doran, J.C., and S. Zhong, 1994: Regional drainage flows in the Pacific Northwest. *Mon. Wea. Rev.*, **122**, 1158-1167. doi.org/10.1175/1520-0493(1994)122<1158:RDFITP>2.0.CO;2

Fosberg, M.A., and M.J. Schroeder, 1966: Marine air penetration in Central California. *J. Appl. Meteor.*, **5**, 573-589. doi:10.1175/1520-0450(1966)<0573:MAPICC>2.0.CO;2.

Fovell, R.G., and A. Gallagher, 2020: Boundary layer and surface verification of the High-Resolution Rapid Refresh, Version 3. . *Wea. Forecasting*, **35**, 2255-2278; doi: 10.1175/WAF-D-20-0101.1

Johnson, A., Jr., and J.J. O'Brien, 1973: A study of an Oregon sea breeze event. *J. Appl. Meteor.*, **12**, 1463-1473, doi.org/10.1175/1520-0450(1973)012<1267:ASOAOS>2.0.CO;2

Kalnay, E., et al. 1996: The NCEP/NCAR 40-Year Reanalysis Project. Bull. Amer. Meteor. Soc., 77, 437–472; doi.org/10.1175/1520-0477(1996)077<0437:TNYRP>2.0.CO;2

Klaas, T., L. Pauscher, and D. Callies, D., 2015: LiDAR-mast deviations in complex terrain and their simulation using CFD. *Meteor. Zeitschrift*. 24. 591-603. Doi:10.1127/metz/2015/0637

Lee, T.R., M. Buban, D. Turner, T.P. Meyers, and C.B. Baker, 2019: Evaluation of the High-Resolution Rapid Refresh (HRRR) model using near-surface meteorological and flux observations from northern Alabama. *Wea. Forecasting*, **34**, 635-663; doi: 10.1175/WAF-D-18-0184.1

Lhermitte, R., and D. Atlas, 1961: Precipitation motion by pulse Doppler radar. Preprints, *9th Radar Meteorology Conf.*, Kansas City, Amer. Meteor. Soc., 218-223.

McCaffrey, K., J.M. Wilczak, L. Bianco, E. Grimit, J. Sharp, R. Banta, K. Friedrich, H.J.S. Fernando, R. Krishnamurthy, L. Leo and P. Muradyan, 2019: Identification and characterization of persistent cold pool

events from temperature and wind profilers in the Columbia River Basin. J. Appl. Meteor. Climatol., 58, 2533–2551; doi.org/10.1175/JAMC-D-19-0046.1

Marquis, M., J. Wilczak, M. Ahlstrom, J. Sharp, A. Stern, J. C. Smith, and S. Calvert, 2011: Forecasting the wind to reach significant penetration levels of wind energy. *Bull. Amer. Meteor. Soc.*, **92**, 1159–1171, https://journals.ametsoc.org/doi/pdf/10.1175/2011BAMS3033.1.

Mass, C.F., M.D. Albright, and D.J. Brees, 1986: The onshore surge of marine air into the Pacific Northwest: A coastal region of complex terrain. *Mon. Wea. Rev.*, **114**, 2602-2627, doi:10.1175/2002MWR2275.1.

Mayor, S.D., 2011: Observations of seven atmospheric density current fronts in Dixon, California. *Mon. Wea. Rev.*, **139**, 1267-1283, doi:10.1175/2010MWR3374.1.

Nakanishi, M., and H. Niino, 2009: Development of an improved turbulence closure model for the atmospheric boundary layer. *J. Meteor. Soc. Japan*, **87**, 895–912. https://doi.org/10.2151/jmsj.87.895.

Neiman, P.J., D.J. Gottas, and A.B. White, 2019: A two-cool-season wind profiler based analysis of westward-directed gap flow through the Columbia River Gorge. *Mon. Wea. Rev.*, **147**, 4653–4680; doi.org/10.1175/MWR-D-19-0026.1

Olson J., J.S. Kenyon, W.M. Angevine, J.M. Brown, M. Pagowski, and K. Sušelj, 2019a: A description of the MYNN–EDMF scheme and coupling to other components in WRF–ARW. NOAA Technical Memorandum OAR GSD, 61, 37 pp., https://doi.org/10.25923/n9wm-be49.

_____, _____, M. Toy, J.M. Brown, W. Angevine, J.-W. Bao, P. Jimenez, B. Kosovic, K. Lundquist, J.K. Lundquist, J. McCaa, C. Draxl, L.K. Berg, and R.M. Banta, 2019b: Model development in support of the Second Wind Forecast improvement Project (WFIP 2). *Bull. Amer. Meteor. Soc.*, **100**, 2201-2220; doi.org/10.1175/BAMS-D-18-0040.1

Olsson, L.E., W.P. Elliott, and S.-I. Hsu, 1973: Marine air penetration in Western Oregon: An observational study. *Mon. Wea. Rev.*, **101**, 356-362. doi:10.1175/2002MWR2275.1

Pichugina, Y.L., R.M. Banta, et al., 2019: Spatial variability of winds and HRRR-NCEP model error statistics at three Doppler-lidar sites in the wind-energy generation region of the Columbia River Basin. *J. Appl. Meteor. Climatol.*, **58**, 1633-1656. doi.org/10.1175/JAMC-D-18-0244.1

_____, _____, W.A. Brewer, L. Bianco, C. Draxl, J. Kenyon, J. K. Lundquist, J.B. Olson, D.D. Turner, S. Wharton, J. Wilczak, S. Baidar, L.K. Berg, H.J.S. Fernando, B.J. McCarty, R. Rai, B. Roberts, J. Sharp, W.J. Shaw, M.T. Stoelinga, and R. Worsnop, 2020: Evaluating the WFIP2 updates to the HRRR model using scanning Doppler lidar measurements in the complex terrain of the Columbia River Basin. *J. Renewable Sustainable Energ*., **12**, 043301. doi: 10.1063/5.0009138

Schroeder, M.J., M.A. Fosberg, O.P. Cramer, and C.A. O'Dell, 1967: Marine air invasion of the Pacific Coast: A problem analysis. *Bull. Amer. Meteor. Soc*., **48**, 802-808.

Skamarock, W.C., 2004: Evaluating mesoscale NWP models using kinetic energy spectra. *Mon. Wea. Rev.*, **132**, 3019-3032, doi.org/10.1175/MWR2830.1

Sharp, J., and C.F. Mass, 2002: Columbia Gorge gap flow: Insights from observational analysis and ultra-high-resolution simulation. *Bull. Amer. Meteor. Soc*., **83**, 1757-1762.

_____, and _____, 2004: Columbia Gorge gap winds: Their climatological influence and synoptic evolution. *Wea. Forecasting*, **19**, 970–992, https://doi.org/10.1175/826.1

Staley, D.O., 1959: Some observations of surface-wind oscillations in a heated basin. *J. Meteor.*, **16**, 364-370.

Thiebaux J., Eric Rogers, Wanqiu Wang, and Bert Katz , 2003: A new high-resolution global sea surface temperature analysis. *Bull. Amer. Meteor. Soc.*, **84**, 645-656.

Wang, M., and P. Ullrich, 2018: Marine air penetration in California's Central Valley: Meteorological drivers and the impact of climate change. *J. Appl. Meteor. Climatol.*, **57**, 137-154. doi:10.1175/JAMC-D-17-0089.1.

Whiteman, C.D., S. Zhong, W.J. Shaw, J.M. Hubbe, and X. Bian, 2001: Cold pools in the Columbia Basin. *Wea. and Forecasting*, **16**, 432-447, doi.org/10.1175/1520-0434(2001)016<0432:CPITCB>2.0.CO;2

Wilczak, J.M., et al., 2019: The Second Wind Forecast Improvement Project (WFIP2): Observational field campaign. *Bull. American Meteor. Soc.*, **100**, 1701-1723; doi.org/10.1175/BAMS-D-18-0035.1

Zaremba, L.L., and J.J. Carroll, 1999: Summer wind flow regimes over the Sacramento Valley. *J. Appl. Meteor.*, **38**, 1463-1473, doi.org/10.1175/1520-0450(1999)038<1463:SWFROT>2.0.CO;2

Zhong, S., C.D. Whiteman, X. Bian, W.J. Shaw, and J.M. Hubbe, 2001: Meteorological processes affecting the evolution of a wintertime cold air pool in the Columbia Basin. *Mon. Wea. Rev.*, **129**, 2600-2613; doi.org/10.1175/1520-0493(2001)129<2600:MPATEO>2.0.CO;2

Tables

Table 1: Event Types for Event Log

Cross Barrier Synoptic	CBS	Westerly gap flow, forced by synoptic pressure gradients
Cross Barrier Thermal	CBT	Westerly gap flow, inland/ocean diurnal heating contrast
Stable Layer	SL	Cold-pool/inversion structure in Basin
Mountain Wave	MW	Mountain lee waves in westerly-component flow over Cascade Mountains
Topographic Wake	TW	Wakes off major peaks (Mt. Hood, Mt. Adams, etc.) observed over Basin
Convective Outflow	CO	Thunderstorm outflows affect winds over Basin
Easterly Flow	EF	Easterly gap flow over WFIP2 area
Other	OT	Unclassifiable flows (e.g., light and variable)

Event Log Briefers during project	Jaymes Kenyon, Robert Banta, Joseph Olson, Justin Sharp, Mark Stoelinga, Eric Grimit, Qing Yang, Kyle Wade, Larry Berg, Eric James
Post-project editing, compilation, and completion:	Justin Sharp, Rochelle Worsnop

Table 2: Doppler Lidar Scan Schedule: Scan sequences continuously performed by lidars every 15-min at the three sites.

	Elevation (°)	**Azimuth (°)**	**Duration (min)**
Scan type	**Wasco**		
Conical (PPI)	2.75, 4,6,15,45	0-360 scanning	8.5
Elevation (RHI)	0-30 scanning	0, 90, 180, 270	3.5
Vert. stare	90	---	3
	Arlington		
Conical (PPI)	1.75, 3, 6, 15, 45	0-360 scanning	8.5
Elevation (RHI)	0-30 scanning	0, 90, 180, 270	3.5
Vert. stare	90	---	3
	Boardman		
Conical (PPI)	1.75, 3, 6, 15, 45	0-360 scanning	6.5
Elevation (RHI)	0-30 scanning	0, 90, 180, 270	8.5
Vert. stare	90	---	3.5

Table 3: Diurnal Wind Regimes, WFIP2 Summer 2016

Regime	Abbreviation	Primary forcing	Quantitative Criteria Applied
Marine Intrusion	Intrsn	Thermal	Max speed > 10 m s^{-1}; Min speed < 3 m s^{-1} at ARL
East-West-East	EWE	Thermal	
Up trending	Up	Synoptic	
Westerly all day	Strong W, or W!	Synoptic	Min speed > 5 m s^{-1} at ARL or BDM
Down trending	Down	Synoptic	Previous day min speed > 5 m s^{-1} at all sites
Cool Diel	CoolDiel	Both (hybrid)	
No Diel	NoDiel	--	

Table 4. Regression variables for lines in Fig. 9.

Dominant Forcing	Regimes	Slope	Intercept	Correlation Coefficient **r**
Thermal/diurnal	Intrusion, EWE	0.7	-1.2	0.93
Large-scale Δp	Up, Strong W, Down	0.8	-7.0	0.61

Table A1. Days Included in Each Wind Regime

Date	Julian	Event Log Type		Date	Julian	Event Log Type
Marine Intrusion				Up-ramping		
28 June	180	CBT		13 June	165	CBS, MW
29 June	181	CBT		18 June	170	CBS, MW, TW
30 June	182	CBT, CBS		22 July	204	CBS, CBT
26 July	208	CBT,CBS		2 Aug	215	CBS,MW,TW
14 Aug	227	CBT, CBS		21 Aug	234	CBT, CBS, TW
15 Aug	228	CBS, CBT		27 Aug	240**	CBS
16 Aug	229	CBS, CBT		30 Aug	243	CBS,MW,TW
17 Aug	230	CBT		Strong W (W!)		
EWE				2 June	154	MW,TW,CBS
5 June	157	SL, EF		8 June	160	CBS,CBT
27 June	179	EF, OT		10 June	162	CBS,CBT
4 Aug	217	EF, OT		11 June	163	CBS,CBT,MW
12 Aug	225	EF		14 June	166	CBS, MW
13 Aug	226	CBT, CBS		16 June	168	CBS, CBT
20 Aug	233	EF		23 June	175	CBS,MW,CBT,TW
24 Aug	237**	CBT, EF		24 June	176	CBS,MW,TW
25 Aug	238**	CBT, EF		2 July	184	CBS, CBT
26 Aug	239**	CBS		3 July	185	CBS, CBT
EWE-plus				4 July	186	CBS, CBT
25 July	207	CBT, OT		10 July	192	CBS,CBT,CO,MW
28 July	210	CBT, EF		11 July	193	CBS,TW,MW,CBT
29 July	211	CBT, EF		12 July	194	CBS,TW,MW,CBT
Cool Diel				30 July	212	CBS, CBT
21 June	173	CBS, CBT		6 Aug	219	TW, CBS
5 July	187	CBT, CBS, MW		7 Aug	220	TW, CBS, MW
6 July	188	CBT,CBS, TW		8 Aug	221	CBS, CBT
7 July	189	CBT, CBS, MW		Down-ramping		
8 July	190	CBT, CBS, MW		3 June	155	CBS, EF, OT
14 July	196	CBT, CBS		9 June	161	CBS, CBT, OT
15 July	197	CBT, CBS, MW		12 June	164	CBS, CBT
16 July	198	CBT, CBS		15 June	167	CBS, OT
19 July	201	CBT, CBS		19 June	171	CBS,EF,MW,OT
1 Aug	214	CBS		25 June	177	CBS,EF,CBT
6 Aug	219	CBS, TW		5 July	187	CBS, CBT, MW
10 Aug	223	CBT, CBS		13 July	195	CBS, MW
11 Aug	224	CBT, EF		23 July	205	CBS, CBT
No Diel				31 July	213	CBS
1 June	153	EF, MW		3 Aug	216	CBS
17 June	169	CBS,EF,CBT,OT		22 Aug	235	CBS,CBT,TW,MW
20 June	172	CBS, CBT, EF		28 Aug	241**	CBS
22 June	174	OT, CBT				
26 June	178	OT, EF				
9 July	191	CO, MW				
18 July	200	EF, CBS, OT				
21 July	203	CBS, EF, OT				
5 Aug	218	CBS, CBT				** = HRRR missing days
19 Aug	232	EF, MW				
29 Aug	242**	CBT,CBS,MW,TW				

Table Captions

Table 1: Event Types for Event Log

Table 2: Doppler Lidar Scan Schedule: Scan sequences continuously performed by lidars every 15-min at the three sites.

Table 3: Diurnal Wind Regimes, WFIP2 Summer 2016

Table 4. Regression variables for lines in Fig. 9.

Table A1. Days Included in Each Wind Regime

Figure Captions

Figure 1. (a) Map of the Columbia River Valley with the location of scanning Doppler lidars denoted by gold-filled circles. Red circles indicate the highest peaks of the Cascade Mountains. (b) Google Earth detailed map of the study area showing locations of two NOAA Doppler scanning lidars (200S) at Wasco (452 m ASL) and Arlington (262 m ASL). The Notre Dame University Halo Streamline XR lidar is located at the Boardman site at 110 m ASL. White line indicates an east-west transect of the study region along the predominant wind directions. The surrounding wind turbines are indicated by the clusters of orange dots. (c) Elevation cross section along the transect line in (b).

Figure 2. Examples of images available from Doppler lidar WFIP2 real-time web page; individual panels on web page could be blown up by users for closer scrutiny. a) Expanded version of time-height cross section of wind speed for last 12 h, updated every 15-min. Plotted data are in the form of arrows, representing wind direction, color coded by wind speed, according to the color scale on the right (0 to 25 m s^{-1}). Vertical axis extends from 0 to 3000 m AGL. b) Zoomed-in version of time-height cross section, where vertical axis runs from 0 to 500 m AGL, and wind-speed scale, from 0 to 12 m s^{-1}. c) Time series of wind speed (upper panel) and speed shear (lower panel). Shown are speeds at 50 (blue), 100 (red), and 150 m (gold) for past 12 h. Lower panel shows shear for the 50-100-m (blue) and 100-150-m (red) layers. Vertical axis is adjusted over the measurement range, the upper here going from 0-14 m s^{-1}, and the lower from -0.02 to +0.04 s^{-1}. d) Vertical profiles to 2 km AGL of wind speed (left) and direction (right), for most recent scans, and for 1-h, 2-h, and 3-h ago. e) Time-height cross sections of hourly HRRR wind speeds (upper panel), lidar-measured speeds (middle), and HRRR minus lidar differences (model error). Parallel blue lines bracket nominal turbine rotor layer (50-150

m). f) Time series of model error averaged over 50-150-m layer, for model forecasts ending at the given hour, for the past 12 h: 0-h (initial conditions), 1-h, 2-h, 3-h, 6-h, and 12-h lead-time forecasts are shown (18-h not available for this HRRR version). Model errors are not seen to systematically increase with forecast lead time, as found by Pichugina et al. (2019).

Figure 3. a) Thin black lines: altimeter setting differences (converted to hPa) between AST and HRI (Δp_{AH}) as a function of hour of the day for each JJA day. Thick black line: average value; thick dotted line: standard deviation. b) Daily mean of Δp_{AH} plotted against maximum daily 50-150-m (AGL) wind speed.

Figure 4. Examples of time-height cross sections for regimes dominated by diurnal thermal forcing. (a) left, center: Time-height cross sections of wind speed (height up to 1 km; wind-speed color bar in m s^{-1}), for two INTRUSION days (14-15 August) at Wasco, Arlington, and Boardman. (b) Example of EWE day: Time-height cross sections for 5 June. Marine intrusions began in late afternoon; UTC is retained for the abscissa so this feature is not split. Pacific Standard Time lags UTC by 8 h. Brown bar indicates approximate nighttime hours.

Figure 5. a) Time series of wind speed at three levels within the rotor layer (50, 100, 150 m AGL, to show shear) for two INTRUSION days (14-15 August) at Wasco, Arlington, and Boardman. b) Time series of mean rotor-layer wind speed (left subpanels) and direction (right subpanels) for the three sites; easterly-component wind speeds have been multiplied by -1. Black dot shows peak wind speed for the day from a westerly-component direction, and red dot shows minimum westerly-component speed (negative values indicate easterly flow). Rotor-layer mean curve shown to illustrate maximum-minimum determination.

Figure 6. Top: examples of an UP and a DOWN day: time series of wind speed at three levels within the rotor layer (50, 100, 150 m AGL) for (2-3 August) at Wasco, Arlington, and Boardman. Bottom row: time series of wind speeds: examples of three STRONG W days (10-12 July) and a DOWN day (13 July). Three levels shown to highlight periods of strong shear.

Figure 7. Time series of mean rotor-layer wind speed: examples of a), b) COOL-DIEL and c), d) NO-DIEL days. As in Fig. 5d, easterly-component wind speeds have been multiplied by -1. Black dots show peak wind for the day, and red dots, minimum westerly-component speed.

Figure 8. Time series of composite-mean rotor-layer wind speed (thick black line) and standard deviation (thin black line) for each 15-min lidar profile measurement interval, composited for each regime.

Figure 9. Hourly altimeter-setting differences (hPa) between AST and HRI (Δp_{AH}) vs. time of day (UTC) composited for each regime, color coded by regime. Solid line: mean value; dotted line: standard deviation.

Figure 10. Daily mean of Δp_{AH} plotted against maximum daily 50-150-m (AGL) wind speed (m s^{-1}), color coded by regime. Colored ellipses show approximate area occupied by each regime. EWE-regime and easterly-flow days each show two symbols, a circle for the maximum westerly-component speed, and a square for the minimum (maximum easterly). Open circles show unclassified days, and circle with dot is for 7 June. Slanted lines show best-fit regression lines for thermal-forcing groups (INTRUSION and EWE) and pressure-gradient forcing ("synoptic") groups (STRONG WESTERLY, UP, and DOWN); regression variables shown in Table 4.

Figure 11. Data points represent daily mean of Δp_{AH} plotted against maximum daily 50-150-m (AGL) wind speed, as in Fig. 10, except a) color coded by 500-hPa height, and b) by daily

maximum temperature recorded at HRI by NWS site. 500-hPa height data are averaged for the Salem OR (SLE), Quillayute WA (UIL) and Spokane WA (OTX).

Figure 12. Time series of the 3-station averaged 500-hPa height (blue) and daily peak temperature at HRI (red) as a function of Julian Day in JJA 2016. Dots indicate 1 July and 1 August on both curves, and INTRUSION days associated with each ridge period are annotated in brown. Data were smoothed over three points.

Figure 13. Reanalysis composites of SLP, 925-hPa temperature (T_{925}), and 500-hPa height (h_{500}) for (top) all 92 days of JJA 2016, and (lower rows) each regime as indicated. Color scale is shown for JJA composite at the top (SLP in hPa, T_{925} in C, and h_{500} in dm), and is the same for each corresponding panel. Images provided by the NOAA/ESRL Physical Sciences Laboratory, Boulder Colorado, from the Web site at http://psl.noaa.gov/.

Figure 14a. Time-height plots of wind speed and model error statistics for INTRUSION regime. Panels for top to bottom: lidar-measured wind speeds, HRRR 3-h forecast of wind speed, model bias, unbiased RMSE, and RMSE.

Figure 14b: Same as Fig. 14b, except time-height plots are of windspeeds and model error statistics for STRONG W regime.

Figure 15. Regime-composited time series of wind speed and model error metrics vs. time of day (UTC) for each regime, as indicated. Top rows: wind speeds measured by lidar (connected symbols / dots) and HRRR simulated (solid lines). Model error plots from top, starting at second row: bias, MAE, RMSE, and unbiased RMSE. Locations of measurements color coded: red: Wasco, blue: Arlington, gold: Boardman, and black: 3-site average.

Figure 16. Regime-composited vertical profiles of lidar-measured wind speed and error metrics for the 3-h lead-time forecast, averaged over all hours of the day. Analyses are for regimes dominated by large-scale pressure-gradient forcing (left grouping) and regimes where thermal-contrast forcing prevailed (right grouping). For each regime, first column represents the lidar measured wind-speed profile (m s^{-1}), then, in order, HRRR-model bias (m s^{-1}), mean absolute error (MAE, m s^{-1}), RMSE (m s^{-1}), unbiased RMSE (m s^{-1}), and relative RMSE (%, relative to the lidar measured wind speed). Profiles are color coded according to location—red: Wasco, blue: Arlington, gold: Boardman, and black: 3-site average. Vertical axes: height in meters.

Figure 17. Top: hourly mean AST-HRI pressure difference for each regime, as in Fig.8, plotted against hour of the day (solid) with corresponding HRRR-model predictions of same (dotted). Bottom: Model error—differences between curves in upper panels. HRRR-vs.-measurement differences were calculated in two ways, because model output was sometimes missing (for individual hours, or six entire days: see Table A1), whereas the lidar data were available for all hours. First, differences of the composite means were calculated, using means over all lidar data and means over available HRRR values (except when HRRR missing for entire day), and the differences plotted for each hour. Second, mean of differences was computed by finding the differences for each hour when both a measurement and a model value were available, and then plotting the mean of these differences for each hour. Both methods are shown in the lower panels of Fig. 16; comparing the two shows a mostly small impact of missing hours.

Figure 18. Scatter diagram of measured maximum daily temperature at HRI vs. HRRR-predicted value, in °F. Color coding indicates regime as defined in Fig. 10. Dash-dotted best fit line: slope = 0.55; intercept = 40°F, and correlation coefficient r = 0.63.

Figures

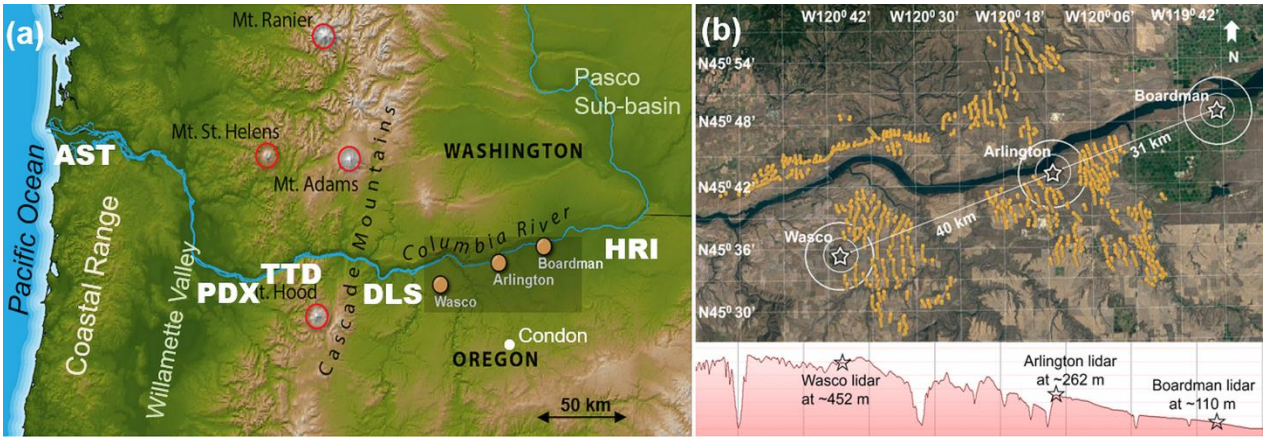

Figure 1. (a) Map of the Columbia River Valley with the location of scanning Doppler lidars denoted by gold-filled circles. Red circles indicate the highest peaks of the Cascade Mountains. (b) Google Earth detailed map of the study area showing locations of two NOAA Doppler scanning lidars (200S) at Wasco (452 m ASL) and Arlington (262 m ASL). The Notre Dame University Halo Streamline XR lidar is located at the Boardman site at 110 m ASL. White line indicates an east-west transect of the study region along the predominant wind directions. The surrounding wind turbines are indicated by the clusters of orange dots. (c) Elevation cross section along the transect line in (b).

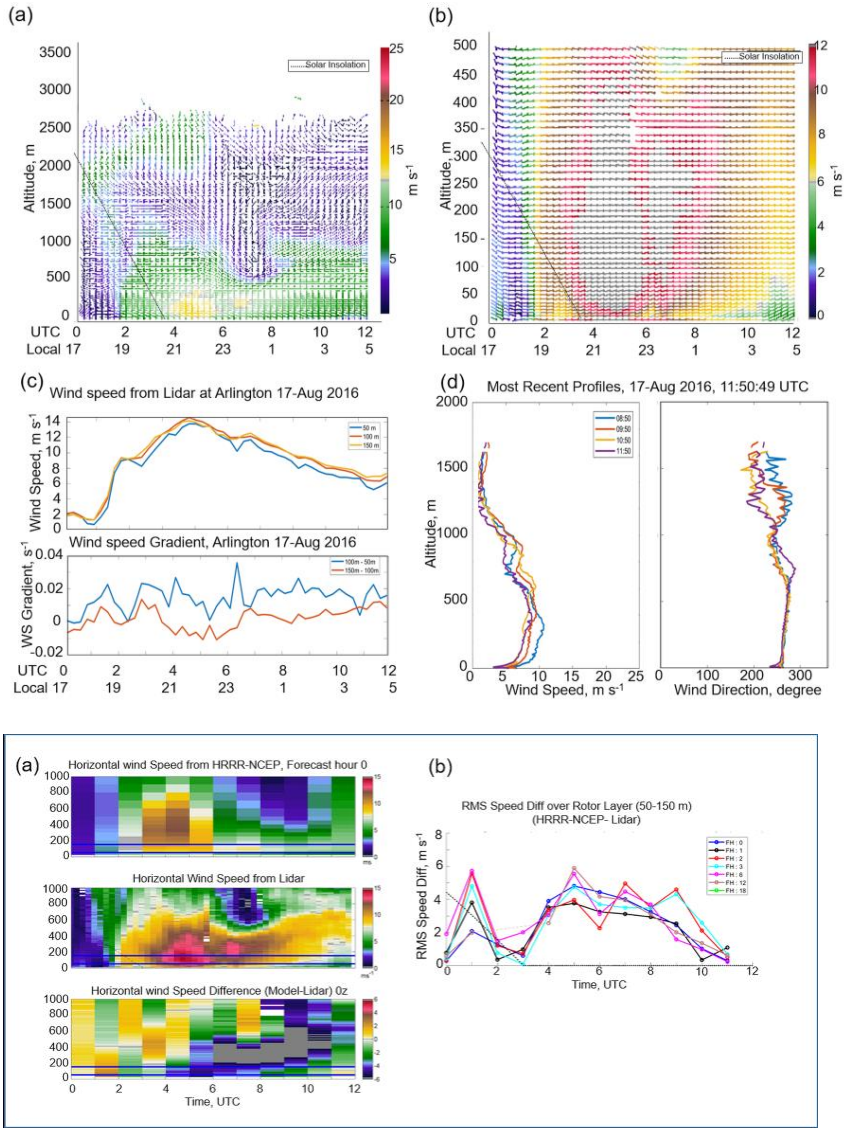

Figure 2. Examples of images available from Doppler lidar WFIP2 real-time web page; individual panels on web page could be blown up by users for closer scrutiny. a) Expanded version of time-height cross section of wind speed for last 12 h, updated every 15-min. Plotted data are in the form of arrows, representing wind direction, color coded by wind speed, according to the color scale on the right (0 to 25 m s^{-1}). Vertical axis extends from 0 to 3000 m AGL. b) Zoomed-in version of time-height cross section, where vertical axis runs from 0 to 500 m AGL, and wind-speed scale, from 0 to 12 m s^{-1}. c) Time series of wind speed (upper panel) and speed shear (lower panel). Shown are speeds at 50 (blue), 100 (red), and 150 m (gold) for past 12 h. Lower panel shows shear for the 50-100-m (blue) and 100-150-m (red) layers. Vertical axis is adjustable over the measurement range, the upper here going from 0-14 m s^{-1}, and the lower from -0.02 to +0.04 s^{-1}. d) Vertical profiles to 2 km AGL of wind speed (left) and direction (right), for most recent scans, and for 1-h, 2-h, and 3-h ago. e) Time-height cross sections of hourly HRRR wind speeds (upper panel), lidar-measured speeds (middle), and HRRR minus lidar differences (model error). Parallel blue lines bracket nominal turbine rotor layer (50-150 m). f) Time series of model error averaged over 50-150-m layer, for model forecasts ending at the given hour, for the past 12 h: 0-h (initial conditions), 1-h, 2-h, 3-h, 6-h, and 12-h lead-time forecasts are shown (18-h not available for this HRRR version). Model errors are not seen to systematically increase with forecast lead time, as found by Pichugina et al. (2019).

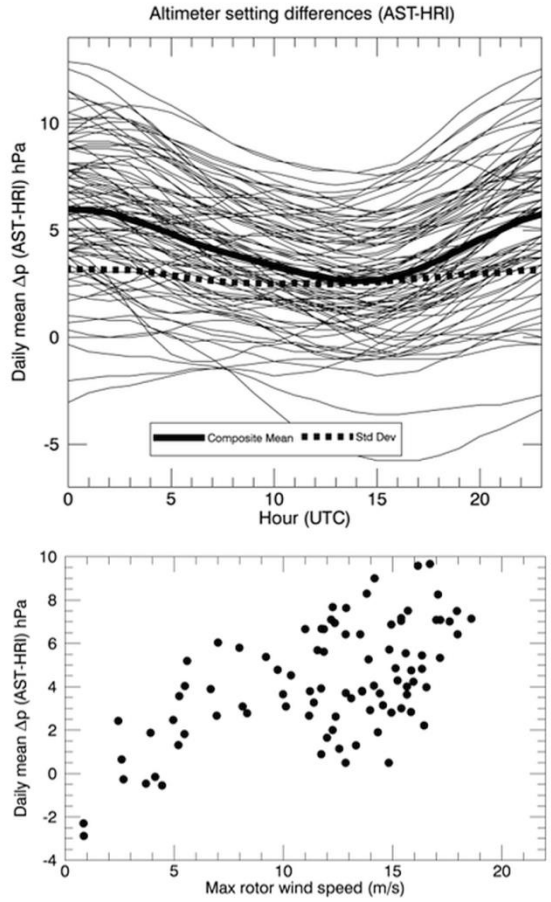

Figure 3. a) Thin black lines: altimeter setting differences (converted to hPa) between AST and HRI (Δp_{AH}) as a function of hour of the day for each JJA day. Thick black line: average value; thick dotted line: standard deviation. b) Daily mean of Δp_{AH} plotted against maximum daily 50-150-m (AGL) wind speed.

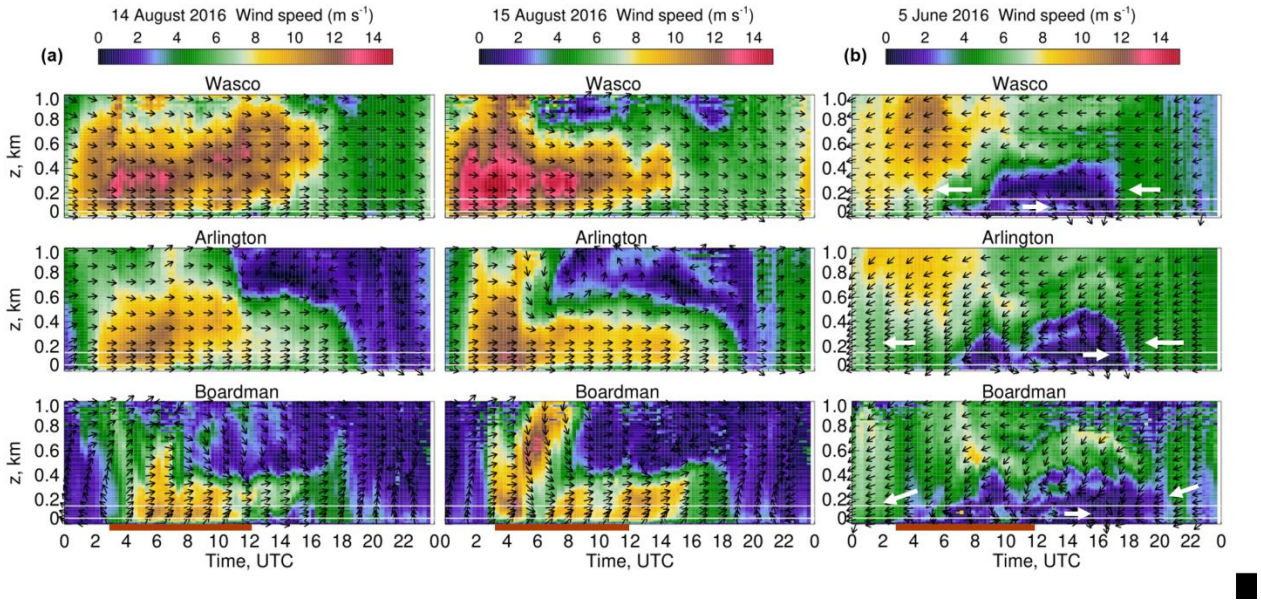

Figure 4. Examples of time-height cross sections for regimes dominated by diurnal thermal forcing. (a) left, center: Time-height cross sections of wind speed (height up to 1 km; wind-speed color bar in m s-1), for two INTRUSION days (14-15 August) at Wasco, Arlington, and Boardman. (b) Example of EWE day: Time-height cross sections for 5 June. Marine intrusions began in late afternoon; UTC is retained for the abscissa so this feature is not split. Pacific Standard Time lags UTC by 8 h. Brown bar indicates approximate nighttime hours.

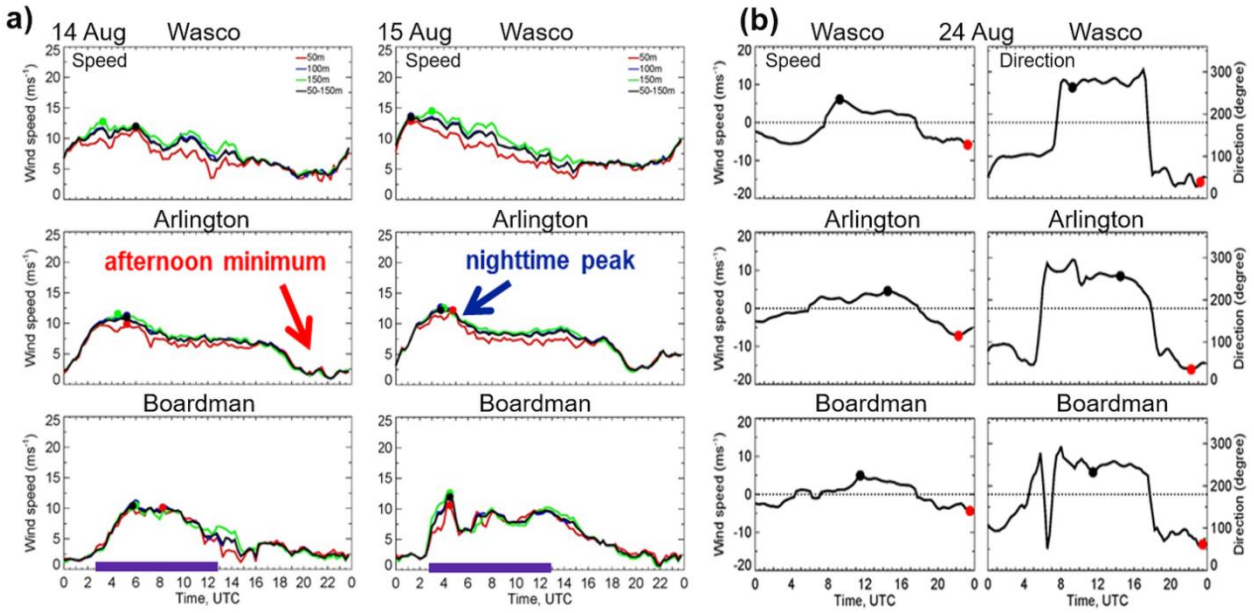

Figure 5. a) Time series of wind speed at three levels within the rotor layer (50, 100, 150 m AGL, to show shear) for two INTRUSION days (14-15 August) at Wasco, Arlington, and Boardman. b) Time series of mean rotor-layer wind speed (left subpanels) and direction (right subpanels) for the three sites; easterly-component wind speeds have been multiplied by -1. Black dot shows peak wind speed for the day from a westerly-component direction, and red dot shows minimum westerly-component speed (negative values indicate easterly flow). Rotor-layer mean curve shown to illustrate maximum-minimum determination.

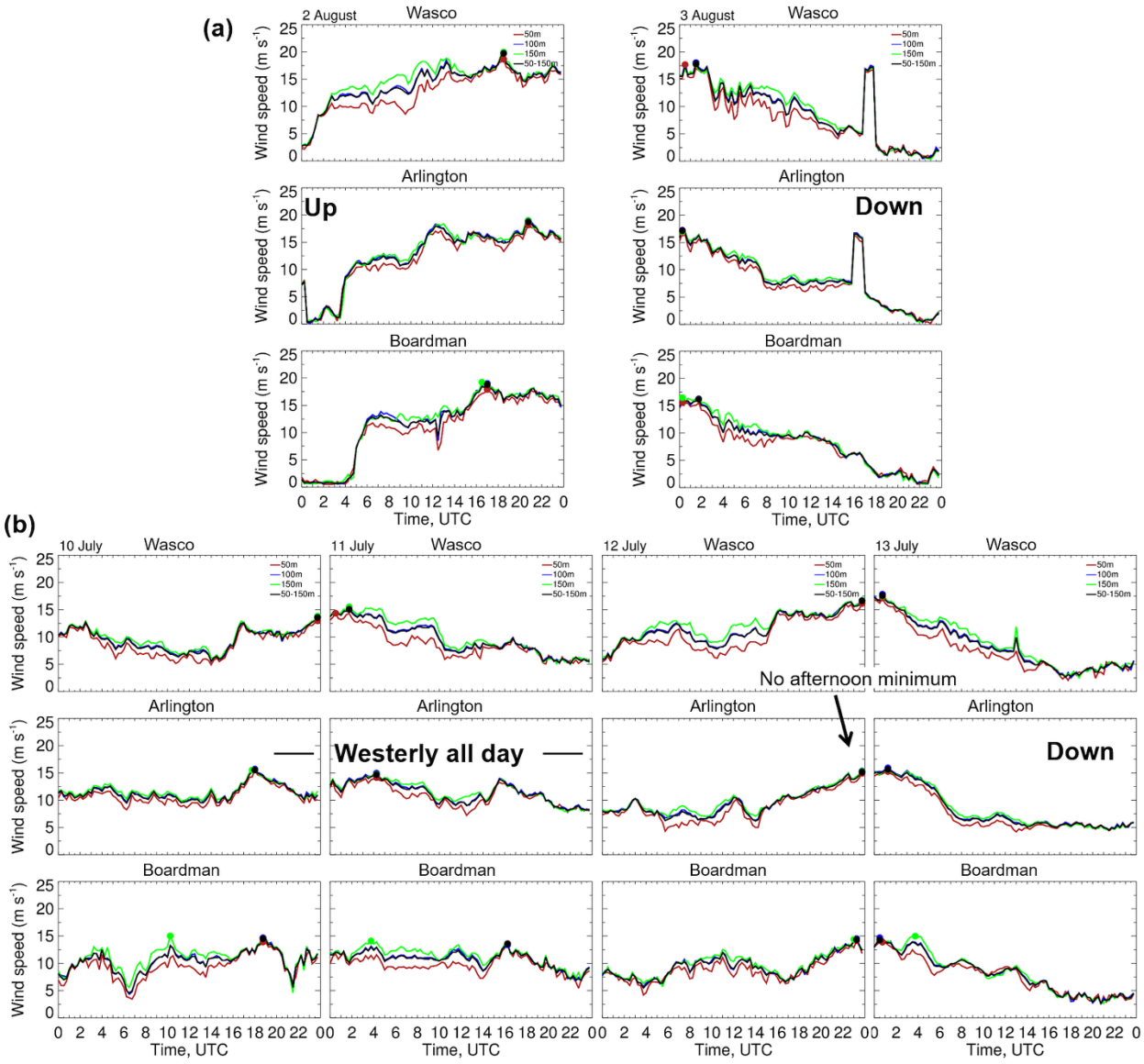

Figure 6. Top: examples of an UP and a DOWN day: time series of wind speed at three levels within the rotor layer (50, 100, 150 m AGL) for (2-3 August) at Wasco, Arlington, and Boardman. Bottom row: time series of wind speeds: examples of three STRONG W days (10-12 July) and a DOWN day (13 July). Three levels shown to highlight periods of strong shear.

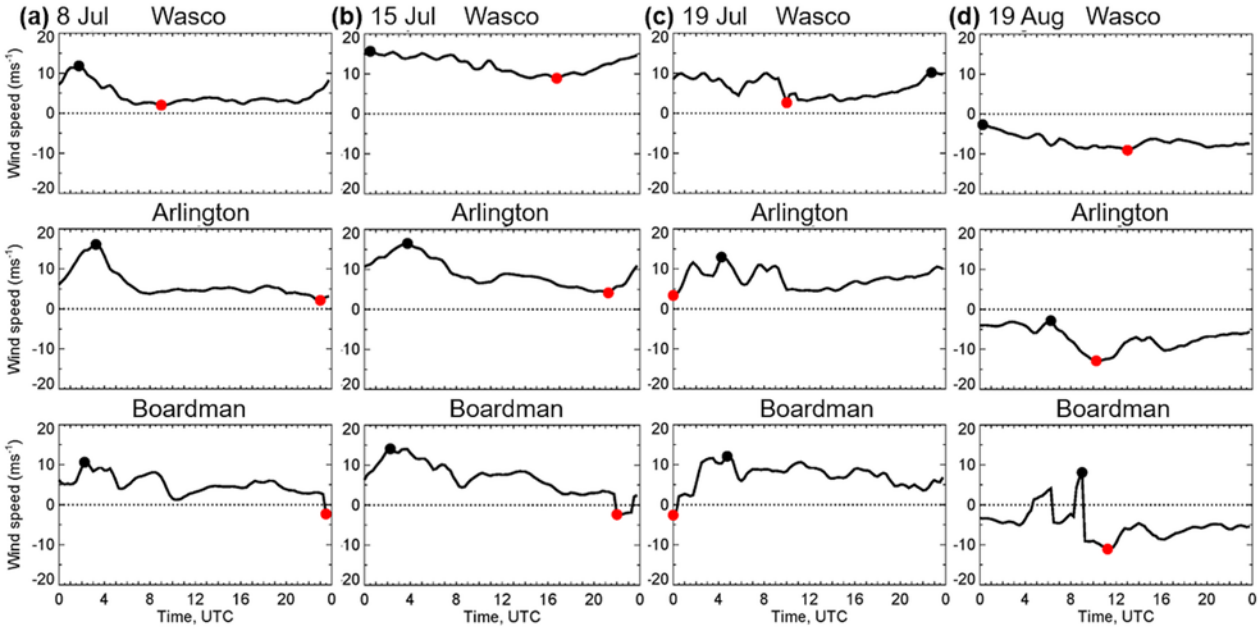

Figure 7. Time series of mean rotor-layer wind speed: examples of a), b) COOL-DIEL and c), d) NO-DIEL days. As in Fig. 5d, easterly-component wind speeds have been multiplied by -1. Black dots show peak wind for the day, and red dots, minimum westerly-component speed.

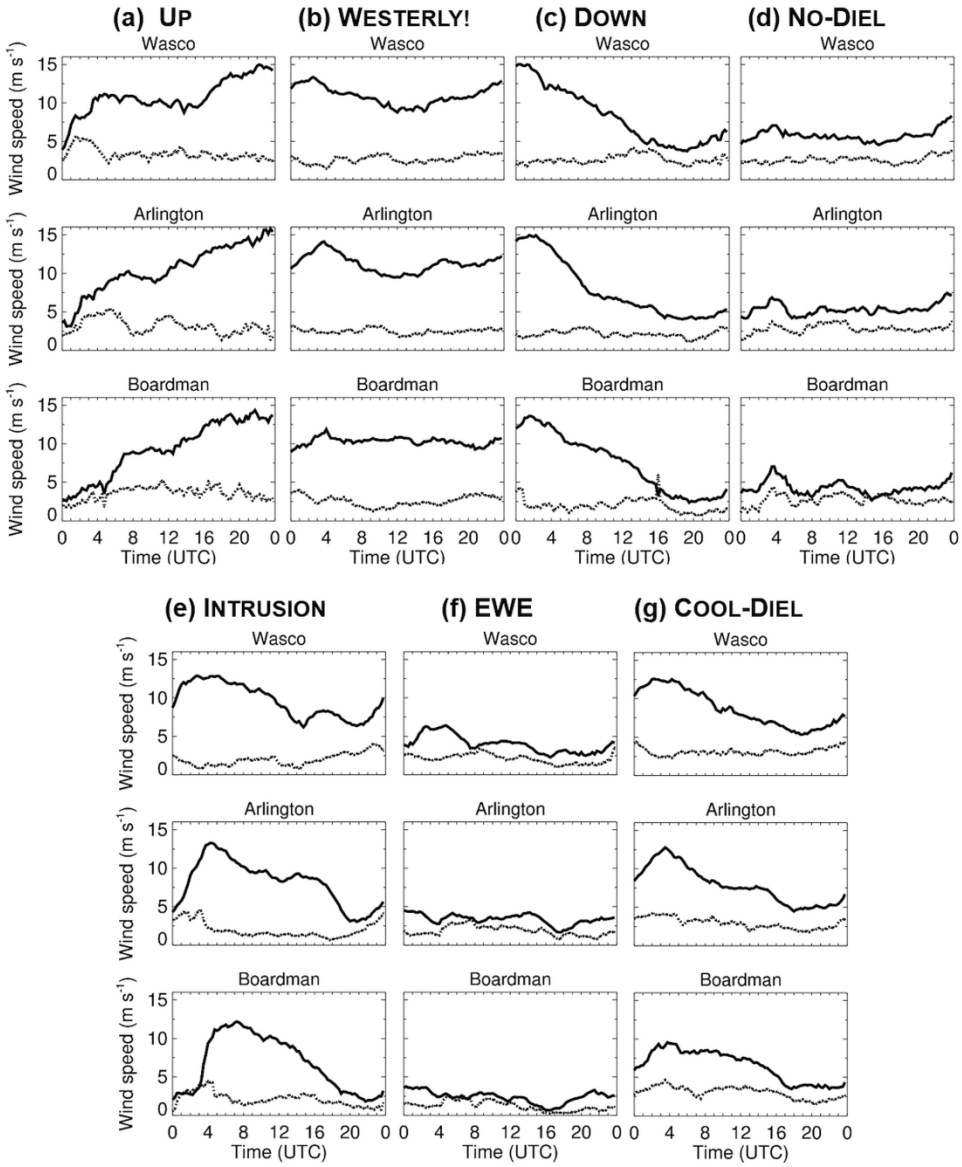

Figure 8. Time series of composite-mean rotor-layer wind speed (thick black line) and standard deviation (thin black line) for each 15-min lidar profile measurement interval, composited for each regime.

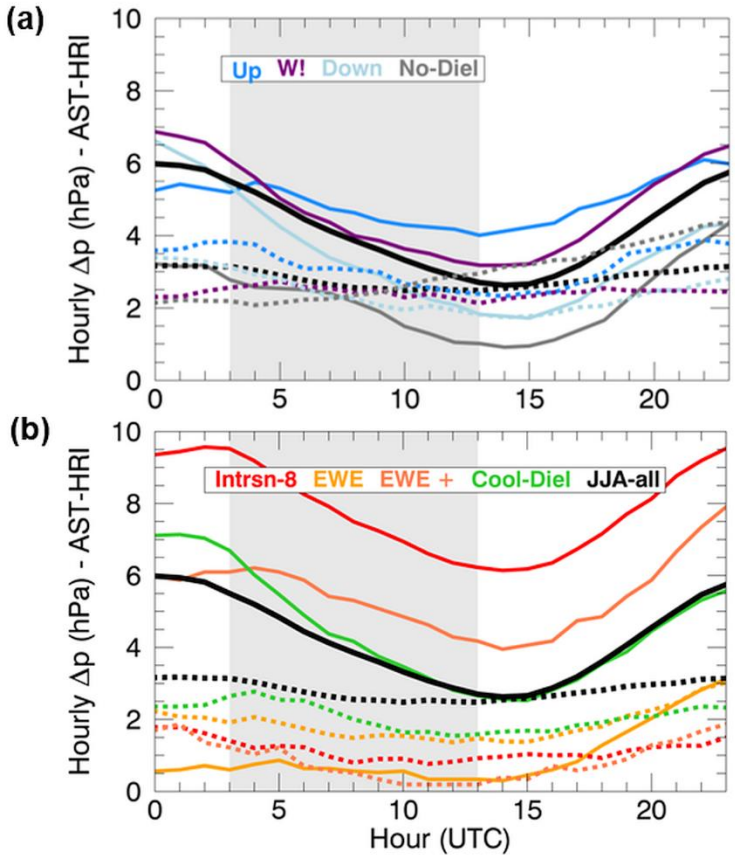

Figure 9. Hourly altimeter-setting differences (hPa) between AST and HRI (Δp_{AH}) vs. time of day (UTC) composited for each regime, color coded by regime. Solid line: mean value; dotted line: standard deviation.

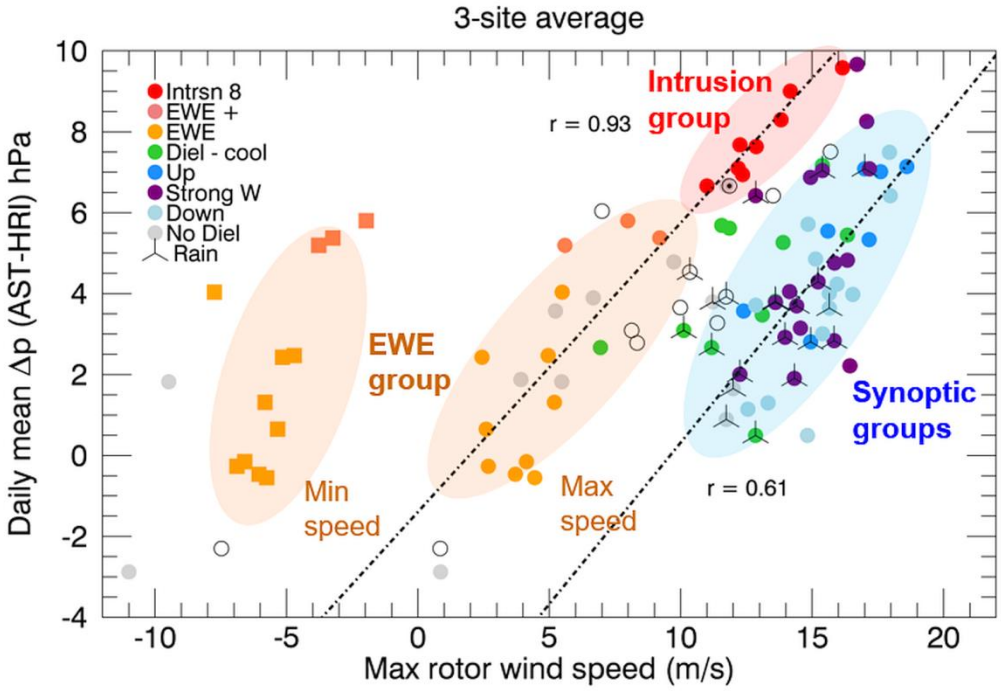

Figure 10. Daily mean of Δp_{AH} plotted against maximum daily 50-150-m (AGL) wind speed (m s^{-1}), color coded by regime. Colored ellipses show approximate area occupied by each regime. EWE-regime and easterly-flow days each show two symbols, a circle for the maximum westerly-component speed, and a square for the minimum (maximum easterly). Open circles show unclassified days, and circle with dot is for 7 June. Slanted lines show best-fit regression lines for thermal-forcing groups (INTRUSION and EWE) and pressure-gradient forcing ("synoptic") groups (STRONG WESTERLY, UP, and DOWN); regression variables shown in Table 4.

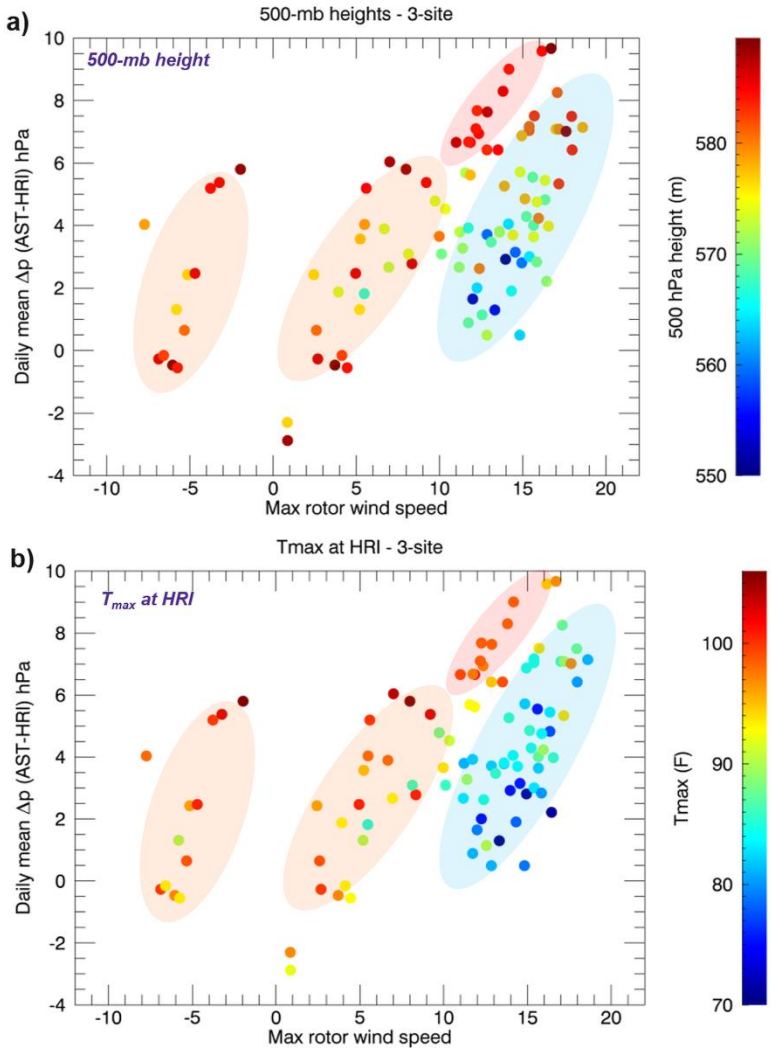

Figure 11. Data points represent daily mean of Δp_{AH} plotted against maximum daily 50-150-m (AGL) wind speed, as in Fig. 10, except a) color coded by 500-hPa height, and b) by daily maximum temperature recorded at HRI by NWS site. 500-hPa height data are averaged for the Salem OR (SLE), Quillayute WA (UIL) and Spokane WA (OTX).

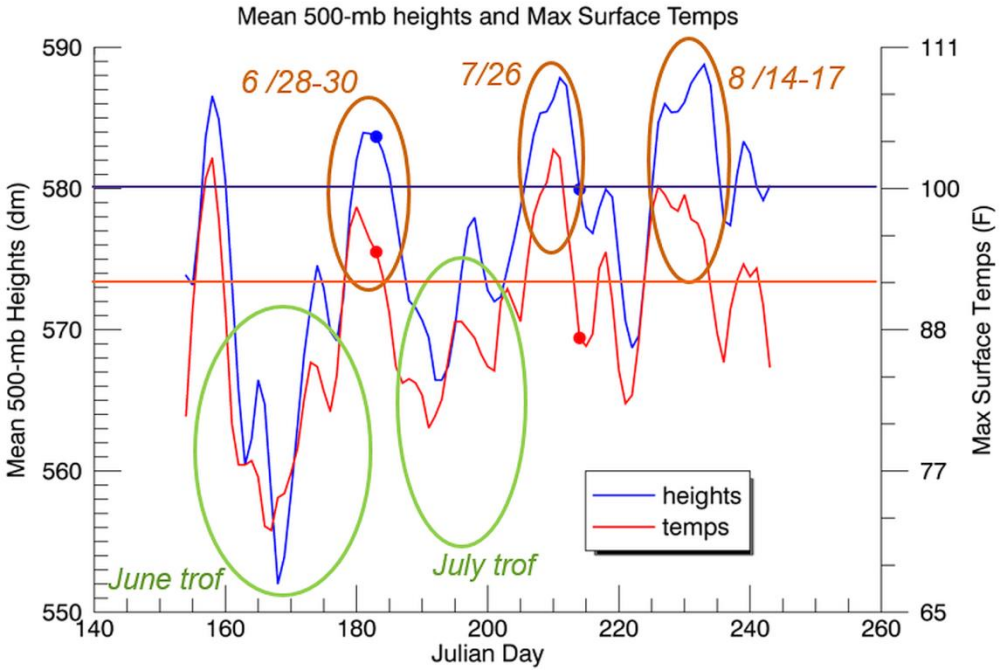

Figure 12. Time series of the 3-station averaged 500-hPa height (blue) and daily peak temperature at HRI (red) as a function of Julian Day in JJA 2016. Dots indicate 1 July and 1 August on both curves, and INTRUSION days associated with each ridge period are annotated in brown. Data were smoothed over three points.

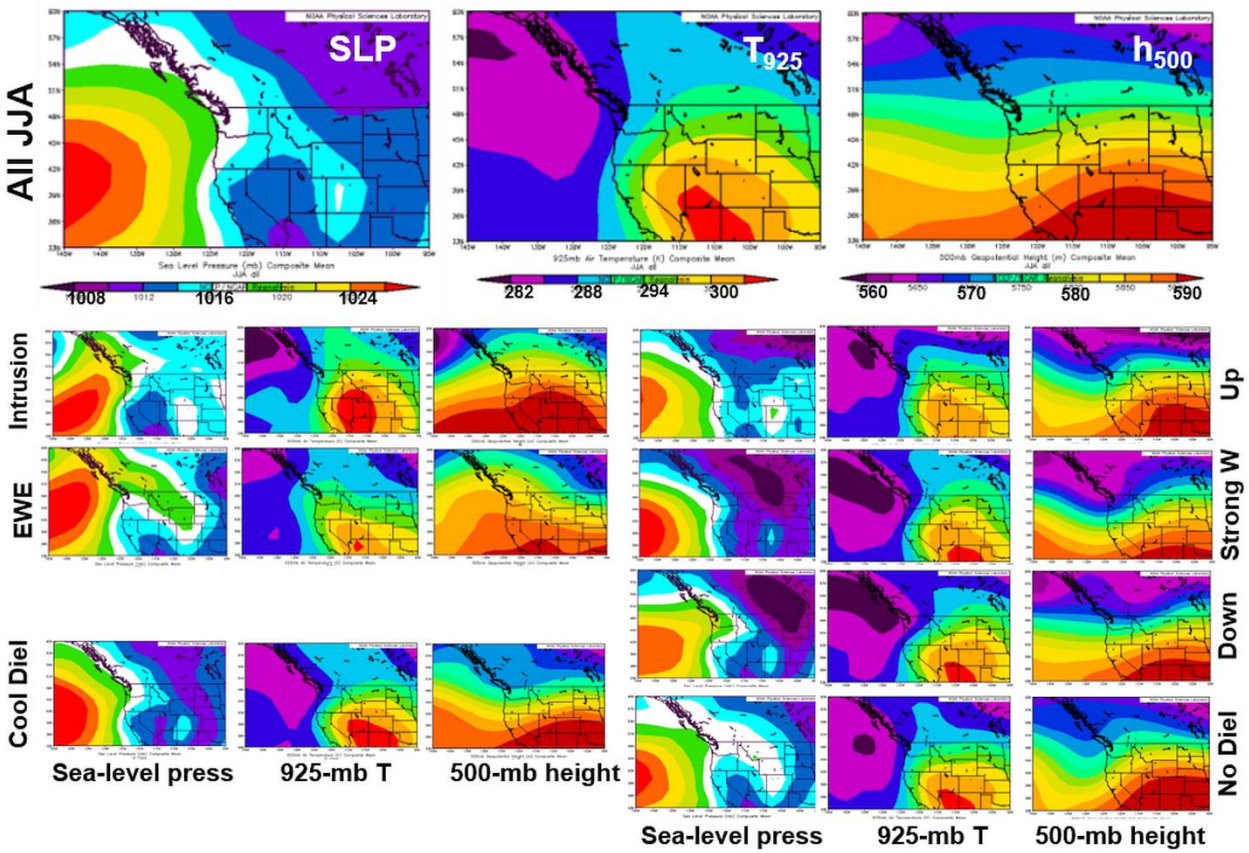

Figure 13. Reanalysis composites of SLP, 925-hPa temperature (T_{925}), and 500-hPa height (h_{500}) for (top) all 92 days of JJA 2016, and (lower rows) each regime as indicated. Color scale is shown for JJA composite at the top (SLP in hPa, T_{925} in C, and h_{500} in dm), and is the same for each corresponding panel. Images provided by the NOAA/ESRL Physical Sciences Laboratory, Boulder Colorado, from the Web site at http://psl.noaa.gov/.

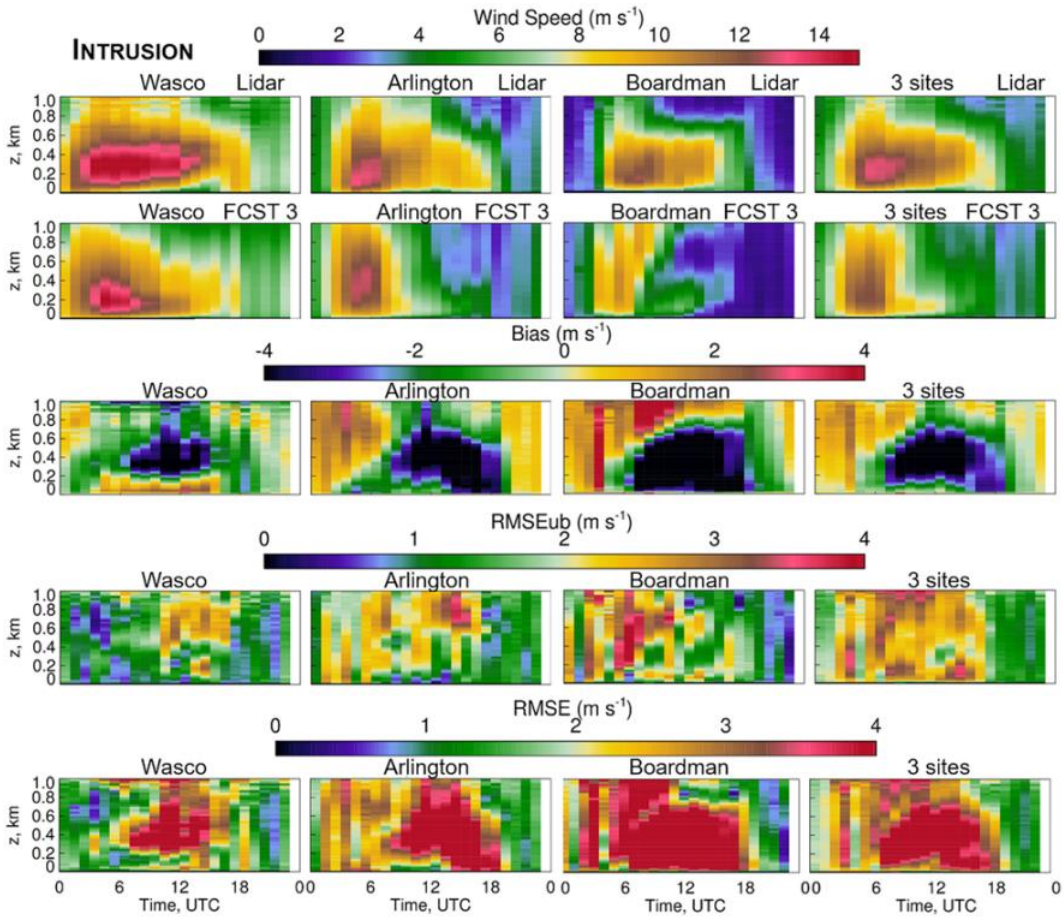

Figure 14a. Time-height plots of wind speed and model error statistics for INTRUSION regime. Panels for top to bottom: lidar-measured wind speeds, HRRR 3-h forecast of wind speed, model bias, unbiased RMSE, and RMSE.

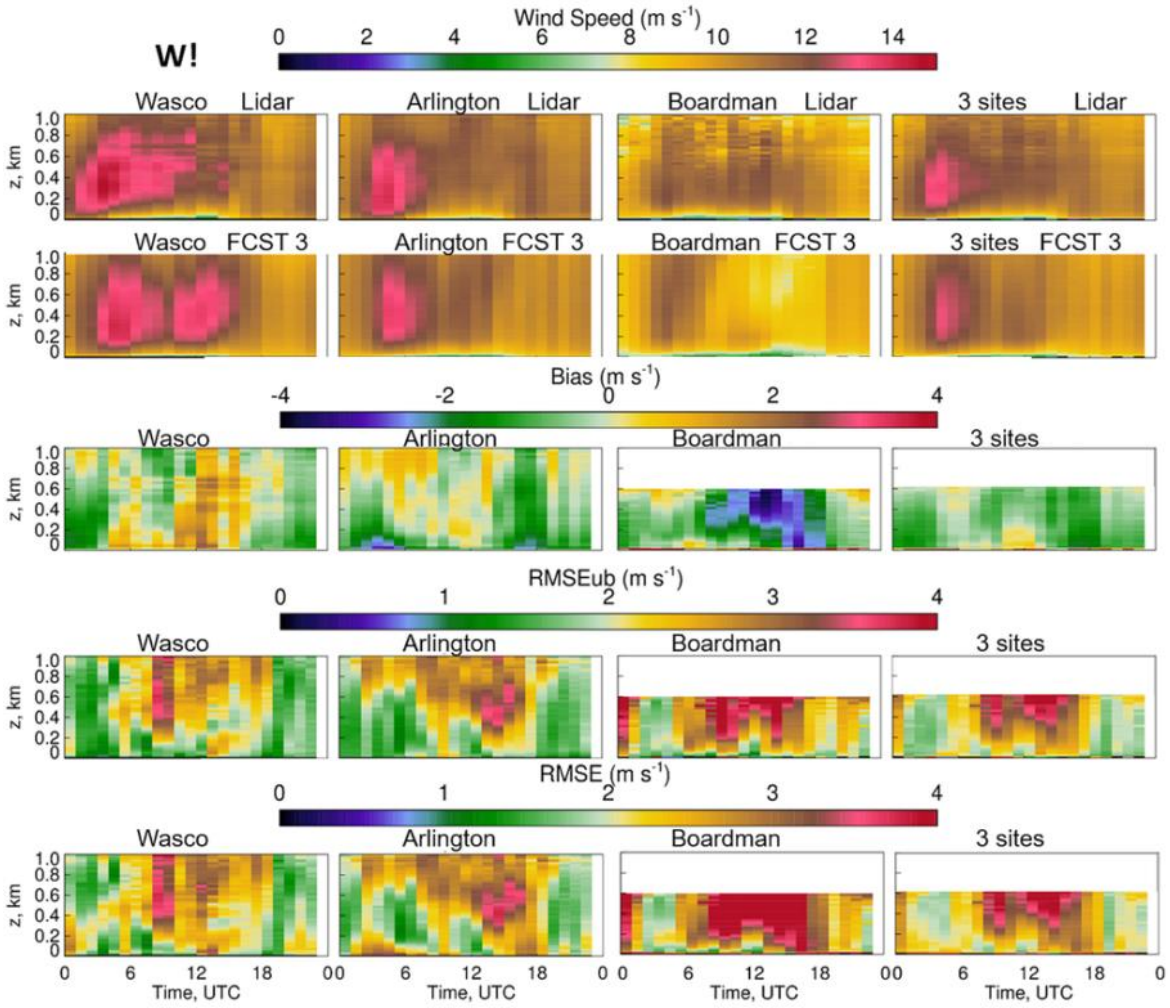

Figure 14b.Same as Fig. 14b, except time-height plots are of windspeeds and model error statistics for STRONG-W regime.

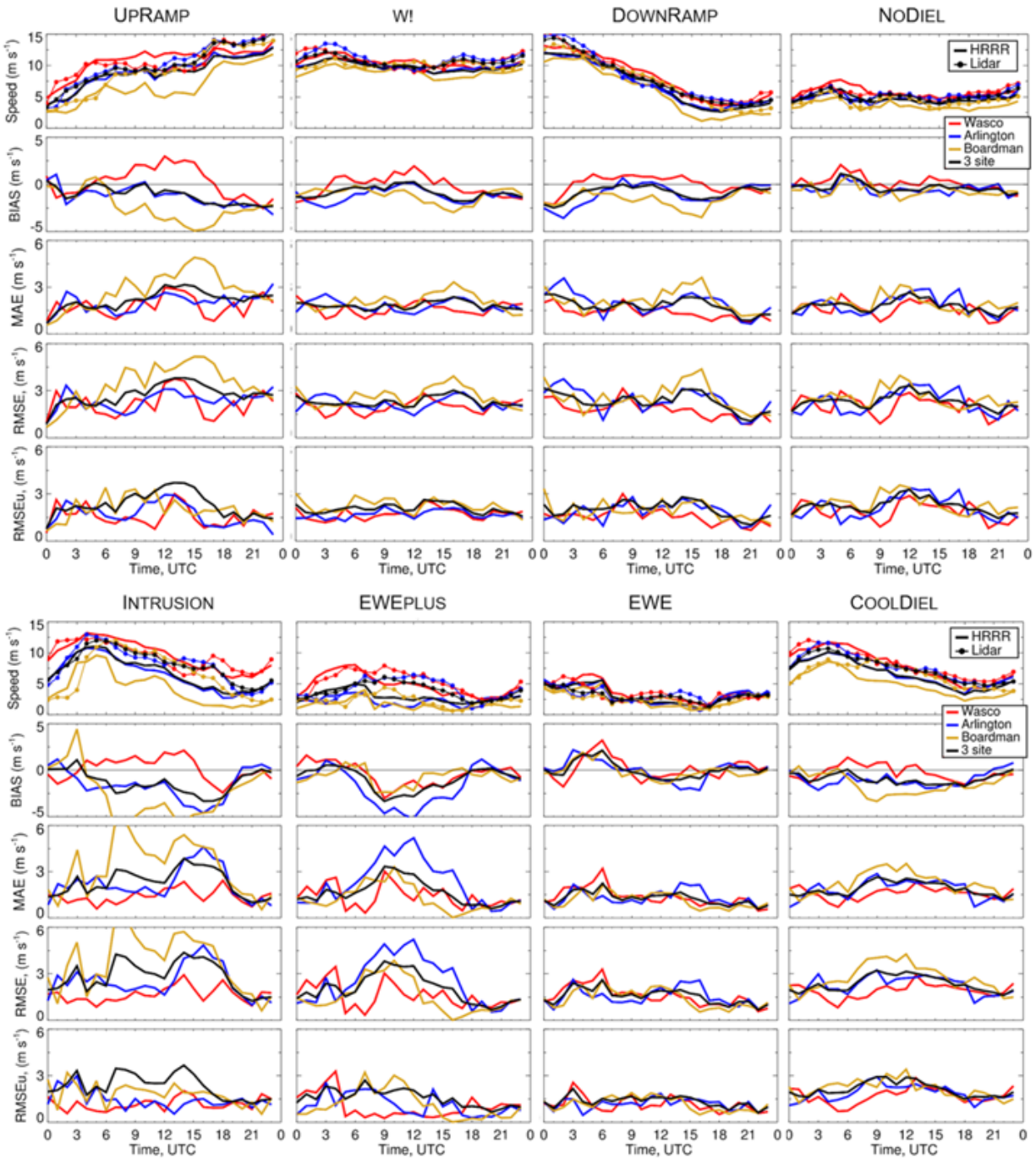

Figure 15. Regime-composited time series of wind speed and model error metrics *vs*. time of day (UTC) for each regime, as indicated. Top rows: wind speeds measured by lidar (connected symbols / dots) and HRRR simulated (solid lines). Model error plots from top, starting at second row: bias, MAE, RMSE, and unbiased RMSE. Locations of measurements color coded: red: Wasco, blue: Arlington, gold: Boardman, and black: 3-site average.

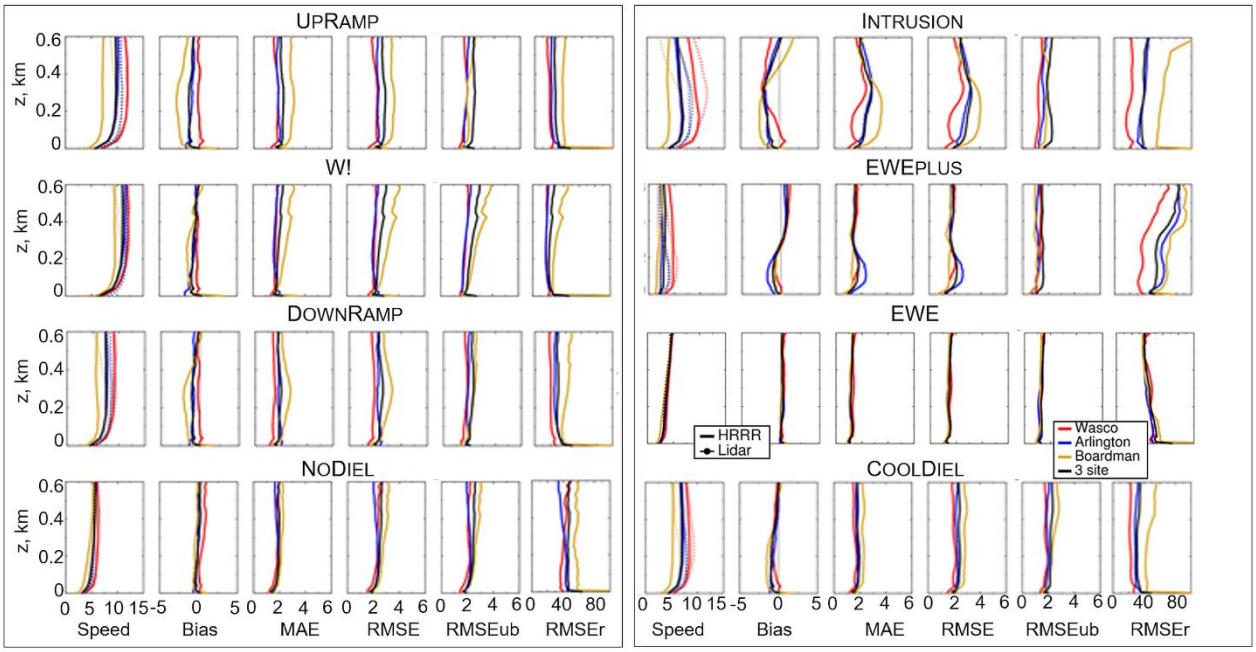

Figure 16. Regime-composited vertical profiles of lidar-measured wind speed and error metrics for the 3-h lead-time forecast, averaged over all hours of the day. Analyses are for regimes dominated by large-scale pressure-gradient forcing (left grouping) and regimes where thermal-contrast forcing prevailed (right grouping). For each regime, first column represents the lidar measured wind-speed profile (m s^{-1}), then, in order, HRRR-model bias (m s^{-1}), mean absolute error (MAE, m s^{-1}), RMSE (m s^{-1}), unbiased RMSE (m s^{-1}), and relative RMSE (%, relative to the lidar measured wind speed). Profiles are color coded according to location—red: Wasco, blue: Arlington, gold: Boardman, and black: 3-site average. Vertical axes: height in meters.

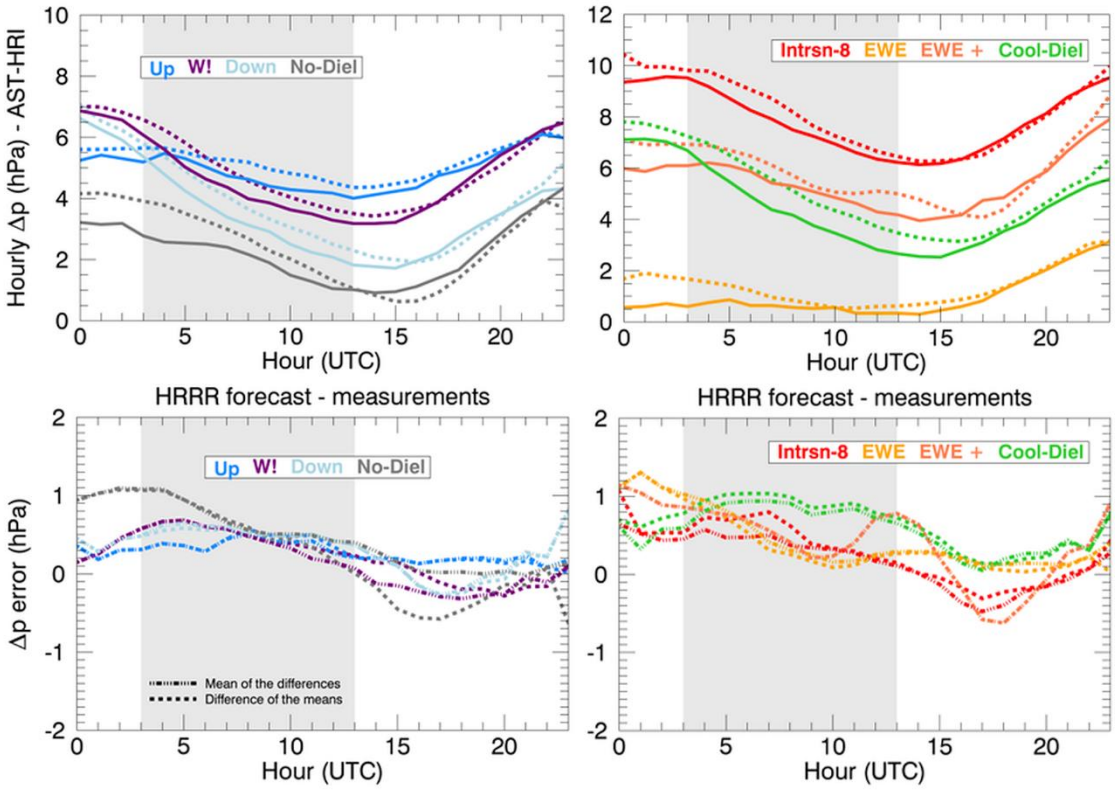

Figure 17. Top: hourly mean AST-HRI pressure difference for each regime, as in Fig.8, plotted against hour of the day (solid) with corresponding HRRR-model predictions of same (dotted). Bottom: Model error—differences between curves in upper panels. HRRR-*vs*.-measurement differences were calculated in two ways, because model output was sometimes missing (for individual hours, or six entire days: see Table A1), whereas the lidar data were available for all hours. First, differences of the composite means were calculated, using means over all lidar data and means over available HRRR values (except when HRRR missing for entire day), and the differences plotted for each hour. Second, mean of differences was computed by finding the differences for each hour when both a measurement and a model value were available, and then plotting the mean of these differences for each hour. Both methods are shown in the lower panels of Fig. 16; comparing the two shows a mostly small impact of missing hours.

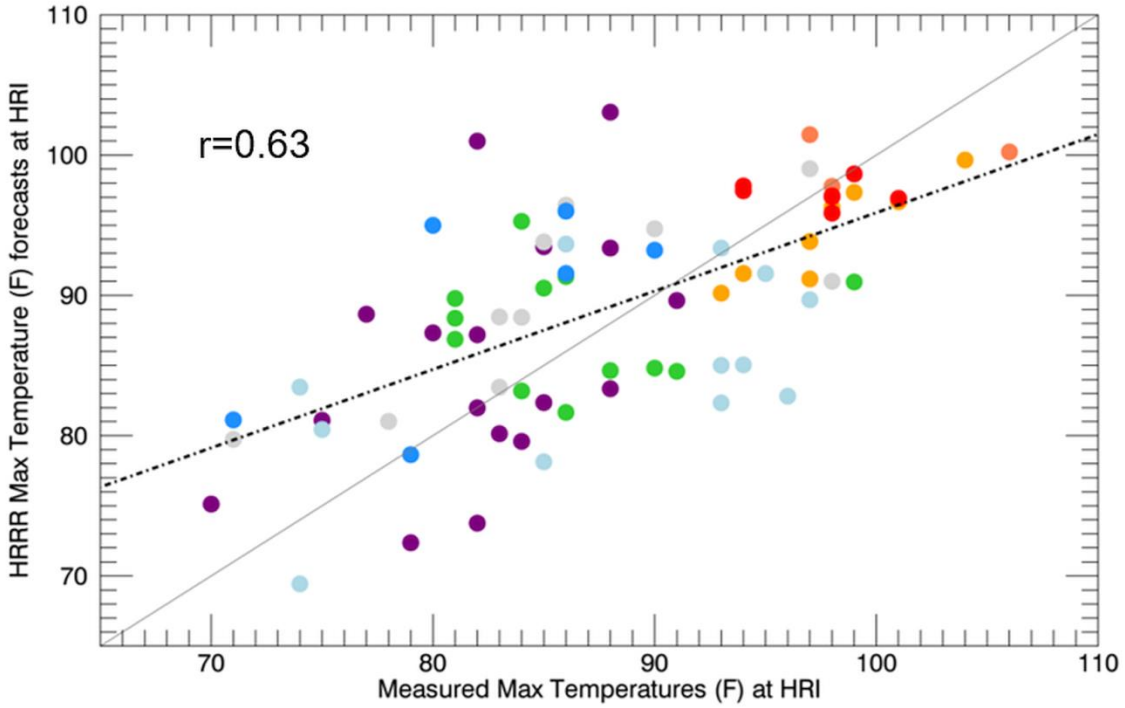

Figure 18. Scatter diagram of measured maximum daily temperature at HRI vs. HRRR-predicted value, in °F. Color coding indicates regime as defined in Fig. 10. Dash-dotted best fit line: slope = 0.55; intercept = 40°F, and correlation coefficient r = 0.63.